



## **Morphological features and water solubility of iron in aged fine aerosol particles over the Indian Ocean**

Sayako Ueda<sup>1</sup>, Yoko Iwamoto<sup>2</sup>, Fumikazu Taketani<sup>3</sup>, Mingxu Liu<sup>1</sup>, Hitoshi Matsui<sup>1</sup>

5 <sup>1</sup> Graduate School of Environmental Studies, Nagoya University, Nagoya, 464-8601, Japan

<sup>2</sup> Graduate School of Integrated Sciences for Life, Hiroshima University, Hiroshima University, Higashi-Hiroshima, 739-8521, Japan

<sup>3</sup> Japan Agency for Marine-Earth Science and Technology, Yokohama, 237-0061, Japan

*Correspondence to:* Sayako Ueda (ueda.sayako.u2@f.mail.nagoya-u.ac.jp)



**Abstract.** Atmospheric transport of iron (Fe) in fine anthropogenic aerosol particles is an important route of soluble Fe supply to remote oceans from continental areas. To investigate Fe properties of aerosol particles over remote oceans, we analyzed atmospheric aerosol particles over the Indian Ocean during the research vessel Hakuho Maru KH-18-6 cruise. Aerosol particles collected using a cascade impactor were analyzed using  
15 transmission electron microscopy (TEM) with an energy-dispersive X-ray spectrometry analyzer. The particle shape and composition on the sample stage of 0.3–0.8  $\mu\text{m}$  aerodynamic diameter indicated that most particles collected north of the equator were composed mainly of ammonium sulfate. Regarding the particle number fraction, 0.6–3.0% of particles contained Fe, which mostly co-existed with sulfate. Of those particles, Fe was found 26% as metal spheres, often co-existing with Al or Si, regarded as fly ash, 14% as mineral dust, and 7%  
20 as iron oxide aggregations. Water-dialysis analyses of TEM samples indicated that Fe in spherical fly ash was almost entirely insoluble, whereas Fe in the other morphological-typed particles was partly (65% Fe mass on average) soluble. Global model simulations mostly reproduce observed Fe mass concentrations in  $\text{PM}_{2.5}$  collected using a high-volume air sampler, including their north–south contrast during the cruise. In contrast, a marked difference was found between the simulated mass fractions of Fe mineral sources and the observed Fe  
25 types. For example, the model underestimated anthropogenic aluminosilicate Fe contained in matter such as fly ash from coal combustion. Our observations suggest that Fe in particles over remote ocean areas has multiple shapes and minerals, and further suggest that its solubility after aging processes differs depending on their morphological and mineral type. Proper consideration of such Fe types at their sources is necessary for accurate estimation of atmospheric Fe effects on marine biological activity.

30



## 1 Introduction

Iron (Fe) is recognized as an essential micronutrient for ocean primary productivity. Addition of water-soluble  
35 Fe to remote oceans, designated as a high-nutrient and low-chlorophyll region, stimulates phytoplankton blooms.  
Iron can thereby change the marine environment and biological diversity, and the global carbon cycle (Martine  
and Fitzwater, 1988; Baar et al., 1995; Harrison et al., 1999; Jickells et al., 2005; Tsuda et al., 2003 and 2007;  
Iwamoto et al., 2009). Transport and deposition of atmospheric aerosol particles is an important route supplying  
Fe to remote ocean areas. Main sources of soluble Fe in the atmosphere are Fe-containing mineral dust and Fe  
40 emitted from anthropogenic combustion and biomass burning (combustion Fe) (e.g. Guieu et al., 2005;  
Mahowald et al., 2009). Mineral dust is emitted mainly as coarse particles by dust storms from arid and semi-  
arid continental areas. By contrast, combustion Fe is emitted as both fine and coarse particles, through  
evaporation and condensation processes (Markowski and Filby, 1985; Liu et al., 2018; Ohata et al., 2018).  
Although many earlier studies have implicated mineral dust as an important source of soluble Fe to oceans (e.g.  
45 Uematsu et al., 1893; Mahowald et al., 2005; Iwamoto et al., 2011), anthropogenic Fe has also attracted  
increasing attention recently as a source supplying water-soluble Fe, steadily and efficiently, by long-range  
transport (Chuang et al., 2005; Sedwick et al., 2007; Luo et al., 2008; Takahashi et al., 2013; Ito, 2015; Matsui  
et al., 2018b).

Recent sophisticated global aerosol modeling studies have evaluated global climatic effects of anthropogenic  
50 Fe (e.g., Scanza et al., 2018; Matsui et al., 2018b; Rathod et al., 2020). Matsui et al. (2018b) demonstrated that  
the atmospheric burden of anthropogenic combustion Fe is eight times greater than earlier estimates. Simulation  
using a soluble Fe mechanism designed for Earth system models by Scanza et al. (2018) incorporates  
consideration of changes of Fe solubility with atmospheric processing of Fe in dust and combustion aerosols.  
They concluded that, in many remote ocean regions, sources of Fe from combustion and dust aerosols are  
55 equally important. Moreover, Rathod et al. (2020) released a revised emission inventory of anthropogenic  
combustion Fe using a technology-based methodology. However, the accuracy of current model-based estimates



remains unclear because of the lack of information related to the mineral composition, morphological structure, and solubility of actual Fe-containing particles in the atmosphere, especially in remote ocean areas.

Actually, Fe is emitted as aerosol particles having various morphologies, with their mineralogy and size  
60 distributions according to their sources. Particle size and composition are related to the particle lifetime and  
water-solubility of Fe. In addition, changes of Fe solubility with particle aging processes depend on many factors  
such as Fe mineralogy and size, atmospheric and meteorological conditions, and particle acidity (Wiederhold  
et al., 2006; Journet et al., 2008; Cwiertny et al., 2008; Shi et al., 2009 and 2015; Ito and Feng, 2010; Li et al.,  
2017; Sakata et al., 2022). Earlier knowledge about relations between solubility, Fe mineral species, and aging  
65 process has usually been based on bulk sample measurements, laboratory experiments, and simulations.  
However, information about individual Fe-containing particles that have experienced actual atmospheric  
transport remains insufficient. To evaluate model results, Fe mass concentrations and solubilities measured  
during numerous observation studies and chemical analyses of bulk samples have been used (Mahowald et al.,  
2009; Wang et al., 2015; Myriokefalitakis et al., 2018; Rathod et al. 2020). Nevertheless, data of bulk samples  
70 alone do not provide information about the source, mineralogy, atmospheric aging, or solubility of individual  
Fe-containing particles. Enhancing our understanding of the roles and effects of atmospheric Fe on marine  
environments necessitates the elucidation of details of atmospheric Fe properties in remote areas far from their  
sources.

Compared to major aerosols such as sea-salt and sulfates, Fe-containing particles constitute a minority in remote  
75 areas. This relative scarcity makes it difficult to find and investigate Fe-containing particles in aerosol samples.  
However, some observation studies conducted in leeward areas of polluted regions have revealed trace metals  
in individual particles (Hidemori et al., 2014; Li et al., 2017). For example, Li et al. (2017) investigated  
individual Fe-containing particles aged for 1–2 days using single-particle analysis of samples collected under  
polluted air over the East China Sea. Using scanning transmission electron microscopy (STEM) and nanoscale  
80 secondary ion mass spectrometry, they demonstrated the presence of iron sulfate in a sulfate coating around



iron oxide ( $\text{FeO}_x$ ) as evidence of Fe aging. Sample collection leeward of polluted regions and recent microscopic techniques has made it possible to find minor Fe in aged particles. As a technique of microscopic analysis, water dialysis is a powerful tool for the investigation of the ratio of water soluble and insoluble materials in individual particles (Okada et al., 1983; Miki et al., 2014; Ueda et al., 2011ab, 2018, 2022). This method comprises  
85 morphological observations and comparison before and after water dialysis of aerosols. Combination with energy-dispersive X ray spectrometry (EDS) can quantify water-soluble elements in individual particles (Ueda et al., 2022).

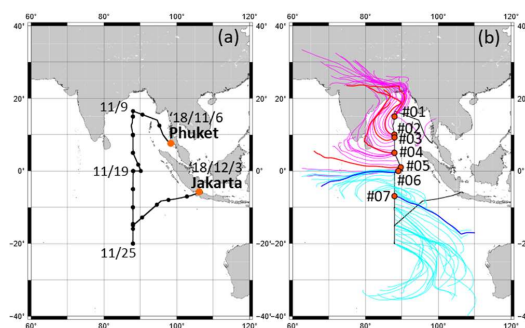
For this study, we conducted sampling to investigate aged Fe-containing particles onboard the R/V Hakuho Maru KH-18-6 cruise of November 2018 over the Indian Ocean. South Asian regions have severe air pollution  
90 problems even now, attributable to anthropogenic and natural sources (Gyttukunda et al., 2014; Chen et al., 2020; Dhaka et al., 2020; Kanawade et al., 2020; Ojha et al., 2020; Takigawa et al., 2020). Sea areas around the KH-18-6 cruise shipping route are not areas with Fe limitations on primary production by marine microorganisms (Mahowald et al., 2018), but are suitable for catching aerosols in long-range transported polluted air from South Asia. By using transmission electron microscopy (TEM) analysis with EDS and water  
95 dialysis in this study specifically examining samples of fine particles that can contain combustion aerosols, we investigated morphological features of Fe-containing particles related to the origin and atmospheric aging process. As basic data for aerosols, bulk aerosol sampling of  $\text{PM}_{2.5}$  was conducted to measure ions and metals. After describing the methods (Sect. 2), this paper presents the mass concentration and number fraction of Fe and their relation with other major aerosol components internally and externally co-existing with Fe, based on  
100 bulk samples and TEM observations (Sects. 3.1 and 3.2). Then, typical morphological features of Fe-containing particles are explained in terms of their relation to the Fe source (Sect. 3.3). Additionally, this report describes global model simulations of each source Fe and comparison with results obtained from observations (Sect. 3.4). Finally, differences of measured solubility for morphologically categorized Fe are presented with discussion of the relation with atmospheric aging and implications from these simulations of Fe (Sect. 3.5).



## 105 2 Methods

### 2.1 Atmospheric observations on board and air mass backward trajectories

Atmospheric observations were conducted over the Indian Ocean during the R/V Hakuho Maru during KH-18-6, which took place on 6–28 November 2018. Figure 1 portrays ship tracks of the R/V Hakuho Maru cruise, 5-day backward air mass trajectories, and sampling locations of TEM samples. The backward trajectories were  
110 computed using the Hybrid Single-Particle Lagrangian Integrated Trajectory (HYSPPLIT) model developed by the National Oceanic and Atmospheric Administration (NOAA) Air Resources Laboratory (ARL) (Stein et al., 2015; Rolph et al., 2017). The settings of the trajectory duration, starting height, vertical mode calculation method, and dataset were chosen, respectively, as 5 days, 500 m above sea level, model vertical velocity, and GDAS meteorological data. Air masses of the northern Indian Ocean (6–16 November 2018) derived from India.  
115 Those around the equator were from the east (6–19 November 2018); those of the southern Indian Ocean were from the sea around western Australia, moving counterclockwise to the observation sites (20–28 November 2018).



120 **Figure 1: Ship tracks of KH-18-06 cruise of the R/V Hakuho Maru (a) and 5-day horizontal backward air mass trajectory (b). Black dots of (a) represent 0:00 am of each day at universal time. Calculations of backward air mass trajectory started from 500 m a.s.l., above the site. Magenta and cyan thin lines respectively show trajectories of every 6 h for sites north and south of the equator. Orange circles of (b) represent TEM sampling sites. Red and blue lines show trajectories for TEM sampling.**



## 2.2 Chemical composition of PM<sub>2.5</sub>

We collected PM<sub>2.5</sub> samples on Teflon filters (WP500-50; Sumitomo Electric Fine Polymer, Inc.) and prebaked  
125 (900 °C for 3 h) quartz fiber filters (QR-100; Advantec Toyo Kaisha Ltd.) using two high-volume samplers  
(HV-700F; Shibata Science Co. Ltd.) with a custom-made particle-size separator at about 12-h or 24-h intervals  
at a flow rate of 500 L min<sup>-1</sup> on the compass deck (a.s.l. 14 m). To avoid collecting particles from the ship  
exhaust (the ship's funnel was located to the rear of the sampling position), the pumping of aerosol samplers  
was controlled automatically using a wind sector to operate only when the relative wind direction was -80° to  
130 80° of the bow and relative wind speed was higher than 3 m s<sup>-1</sup>. After collection, the Teflon and quartz fiber  
filter samples were stored respectively at 4 °C and -18 °C before chemical analyses (for ionic species and trace  
metals) at the home laboratory. Mass concentrations of water-soluble ionic species (Cl<sup>-</sup>, NO<sub>3</sub><sup>-</sup>, SO<sub>4</sub><sup>2-</sup>, Na<sup>+</sup>, NH<sup>+</sup>,  
K<sup>+</sup>, Mg<sup>2+</sup>, and Ca<sup>+</sup>) on quartz fiber filter samples were analyzed using ion chromatography. Non-sea-salt (nss)  
concentrations of SO<sub>4</sub><sup>2-</sup>, K<sup>+</sup>, and Ca<sup>+</sup> were estimated from Na<sup>+</sup> concentrations in the samples using the bulk  
135 seawater ratios described by Wilson (1975). Metals in PM<sub>2.5</sub> (Na, Al, K, Ca, Ti, V, Mn, Fe, Ni, and Zn) were  
analyzed using inductively coupled plasma mass spectrometry (ICP-MS, 7700X, G3281A; Agilent  
Technologies, Inc.) with microwave-assisted extraction in a mixture of nitric acid, hydrofluoric acid, and  
hydrogen peroxide using the Teflon filter sample.

## 2.3 Individual particle analyses using an electron microscope

### 140 2.3.1 Observation and elemental analysis

Aerosol particles were collected for morphological particle analysis using TEM. Aerosols after diffusion drying  
were collected on carbon-coated nitrocellulose (collodion) films using cascade impactors. The 50% cut-off  
diameters of the three stages 1, 2, and 3 were, respectively, 1.6 μm, 0.8 μm, and 0.3 μm. Aerosol samples were  
collected at the upwind side on the compass deck of the ship for 10–30 min at a flow rate of 1.0 L min<sup>-1</sup>. The



145 TEM samples were taken at about 1–2 samples per day and were stored under dry conditions at room temperature (about 25°C) until TEM analyses were conducted at Nagoya University. For this study, seven samples (#01–07) of stage 3 were used for analyses. Sample collection sites and the 5-day backward trajectories are depicted in Fig. 1b. Sample details are presented in Table 1.

**Table 1: TEM samples used for this study and analyzed particle and Fe-containing particle numbers**

Sample ID	Sampling time		Location		Atmospheric conditions		EDS analyzed particles	Fe-containing particles	
	start time	period	Lat.	Long.	Temp.	RH		number	%
	YYYY/MM/DD h:mm	min	N deg.	E deg.	°C	%	number	number	%
#01	2018/11/10 2:43	10	14.99	87.99	28.8	66	535	3	0.6
#02	2018/11/12 1:51	10	10.02	87.98	28.9	81	305	2	0.7
#03	2018/11/13 2:01	20	9.24	88.00	28.8	80	703	17	2.4
#04	2018/11/14 2:36	20	5.01	87.98	28.8	74	507	10	2.0
#05	2018/11/16 2:31	20	1.01	89.72	29.5	69	336	10	3.0
#06	2018/11/18 8:05	25	-0.01	89.06	32.3	60	136	2	1.5
#07	2018/11/21 7:56	31	-6.92	88.00	29.3	71	106	1	0.9

150

Particles collected on the collodion film were photographed using TEM (200 keV, JEM-2100 plus; JEOL Ltd.) at 1.2 k and 6 k × magnifications. To measure the heights of individual particles on the collection surface, particles were coated with a Pt/Pd alloy at a shadowing angle of 26.6° (arctan 0.5) before being micrographed.

155 The Pt/Pd coating thickness was about 7 Å. The EDS analyses were conducted using the TEM operated in





STEM mode at 200 keV. Similar analyses of TEM and EDS hyperspectral imaging (HSI) data were described by Ueda et al. (2020 and 2022) and by Ueda (2021). For this study, EDS-HSI data were sampled at greater than 20 k magnification for 10–30 frames (20 s per frame) and were kept for each dot of  $256 \times 256$  pixels using software (NSS3; Thermo Fisher Scientific Inc., Hampton, NH, USA). The dot size was  $26 \times 26$  nm in the  
160 observed field at 20 k magnification. Although estimation of the mass of each element from EDS analysis is difficult, software can estimate the mass fraction ( $MF_X$ ) of an element  $X$  to all analyzed elements from measurement results of  $X$ -ray counts as relative values to detected elements. Elemental analyses were conducted fundamentally for C, N, O, Na, Mg, Al, Si, P, S, Cl, K, Ca, Ti, V, Mn, Fe, Cu, Zn, Pd, and Pt. Although the software can identify another element automatically if EDS spectra have a specific  $X$ -ray peak, other elements  
165 were detected only rarely. To obtain the elemental compositions of individual particles, the  $MF_X$  of each element was obtained manually for selected areas according to the particle shape and size of each. Noise effects of the background were eliminated using mass normalized by the Pd mass ( $X/Pd$ ) estimated as a ratio of  $MF_X$  to mass fraction of Pd ( $MF_{Pd}$ ). Actually, Pd vapor-deposited to the whole top surface of samples at the shadowing method is not included in general aerosols. In addition, samples #01–07 were vapor-deposited by Pt/Pd at one  
170 time. The  $X/Pd$  can be treated as an independent value from the other components of aerosol, collodion film thickness, and distance from the Cu grid. If the difference of the  $X/Pd$  value of a particle area to that of a near background area was greater than three standard deviations of multiple background spectra in the same sample, then the value was treated as a significant spectrum of the particle.

### 2.3.2 Water dialysis and estimation of water-soluble Fe fraction ( $f_{wsFe}$ )

175 For samples collected from the Indian Ocean (samples #01–#05) north of the equator, a water dialysis technique (Mossop, 1963; Okada, 1983; Okada et al., 2001; Ueda et al., 2011ab, 2018, 2022) was applied to investigate the mixing states of water soluble and insoluble materials in particles. The TEM grid with particle samples was floated on ultrapure water at about 25°C for 3 h with the collection side upward. After water dialysis, some



areas were photographed again. However, a large part of the collodion film unfortunately tore during water  
180 dialysis. For sample #03 only, some EDS analysis data for Fe-containing particles were obtained from the same  
particle area after water dialysis.

Using the Fe mass normalized by Pd mass ( $Fe/Pd$ ) before and after water dialysis of sample #03, the fraction  
of water-soluble Fe to total Fe in individual Fe-containing particles,  $f_{WSFe}$ , was estimated. The fraction of water-  
soluble Fe to total Fe in a particle,  $f_{WSFe}$  can be represented as

185

$$f_{WSFe} = \left(1 - \frac{m_{WIFe}}{m_{Fe}}\right) \times 100 [\%], \quad (1)$$

where  $m_{WIFe}$  and  $m_{Fe}$  respectively denote the masses of water-insoluble Fe and total Fe. For this study, these  
values can be represented respectively as Fe masses after and before water dialysis. Because vapor-deposited  
190 Pd is water insoluble, the mass of Pd after water dialysis can be regarded as unchanged from that before water  
dialysis. In this case, the ratio of  $m_{WIFe}$  and  $m_{Fe}$  of a Fe-containing particle can also be replaced by the ratio of  
 $Fe/Pd$  before and after water dialysis for the same region ( $Fe/Pd_{before}$  and  $Fe/Pd_{after}$ , respectively) as

195

$$f_{WSFe} = \left(1 - \frac{Fe/Pd_{after}}{Fe/Pd_{before}}\right) \times 100 [\%], \quad (2)$$

which comprises only values that were measurable using EDS analysis in this study. Details of this estimation  
method are explained in Supplement S1.

#### 2.4 Global model simulation of Fe

We conducted global model simulations using the Community Atmosphere Model (ver. 5; CAM5) with the  
200 Aerosol Two-dimensional bin module for foRmation and Aging Simulation (ver. 2; CAM5-chem/ATRAS2),



with modifications for particulate iron (Matsui et al., 2014, 2018a; Matsui and Mahowald, 2017; Matsui, 2017; Liu and Matsui, 2021a, 2021b; Liu et al., 2022). Model setting for this study was described by Liu et al. (2022). Briefly, the model incorporates emissions, gas-phase chemistry, condensation or evaporation of inorganic and organic species, coagulation, nucleation, activation of aerosols and evaporation from clouds, aerosol formation  
205 in clouds, dry and wet deposition, aerosol optical properties, aerosol–radiation interactions, and aerosol–cloud interactions. Aerosol particles were resolved with 12 size bins from 0.001 to 10  $\mu\text{m}$  dry diameter. The model was run with horizontal resolution of  $1.9^\circ \times 2.5^\circ$  and 30 vertical layers from the surface to approximately 40 km. The near-surface layer of model results was used for this study.

The model explicitly treats Fe from biomass burning and anthropogenic combustion. Five Fe sources/minerals  
210 (biomass burning, and four anthropogenic Fe (magnetite ( $\text{Fe}_3\text{O}_4$ ), hematite ( $\text{Fe}_2\text{O}_3$ ), kaolinite ( $\text{Al}_2\text{Si}_2\text{O}_5(\text{OH})_4$ ) and illite ( $(\text{K}, \text{H}_3\text{O})(\text{Al}, \text{Mg}, \text{Fe})_2(\text{Si}, \text{Al})_4\text{O}_{10}$ )) are considered in addition to eight other aerosol species (sulfate, nitrate, ammonium, dust, sea salt, primary and secondary organic aerosol, BC, and water). The anthropogenic Fe emission inventory developed by Rathod et al. (2020) with the update by Liu et al. (2022) for Southern Africa was used to model global-scale atmospheric iron concentrations. The size distribution of anthropogenic Fe was  
215 referred from observation results reported by Moteki et al. (2017) for magnetite over eastern Asia from aircraft measurements using a single-particle soot photometer. Combustion iron emissions from open biomass burning were calculated based on Luo et al. (2008). Dust Fe was not treated in our model, but we assumed a constant iron content of 3.5% in natural dust (Duce et al., 1991; Jickells et al., 2005; Shi et al., 2012).

### 3 Results and Discussion

#### 220 3.1 Horizontal variation of $\text{PM}_{2.5}$ components

Figure 2 shows horizontal distributions of  $\text{nss-SO}_4^{2-}$ ,  $\text{NH}_4^+$ , and Fe in  $\text{PM}_{2.5}$ . Average, 25th percentile, and 75th percentile mass concentrations of ions and metals north and south of the equator at  $87\text{--}90^\circ\text{E}$  are presented



respectively in Tables 2 and 3. Scatter plots showing concentrations of Fe and the other elements are supported in Figs. S1 and S2 of Supplemental Materials. Among the measured ions in  $PM_{2.5}$ , the sum of the mass fractions of  $nss-SO_4^{2-}$ ,  $NH_4^+$ ,  $Na^+$ , and  $Cl^-$  was larger than 84% of total ion mass concentrations. North of the equator,  $nss-SO_4^{2-}$  and  $NH_4^+$  concentrations were especially high. These mass fractions were, respectively, 70–76% and 18–22%, except for data of 11 November 2018 when rain events occurred. The values of  $nss-K^+$ , which are regarded as originating mainly from biomass burning (Andreae, 1983; Kawamura and Kaplan, 1987; Narukawa et al., 1999), also tended to be north of the equator. South of the equator, the  $nss-SO_4^{2-}$  and  $NH_4^+$  concentrations were lower. Consequently, the fractions of sea salt components (i.e.  $Na^+$  and  $Cl^-$ ) increased. The  $PM_{2.5}$  ionic amount in equivalent concentrations of total cation without  $H^+$  were comparable to or greater than 75% of that of total anion (Fig. S1a). For non-sea-salt components, the relations between the doubled  $nss-SO_4^{2-}$  molar concentration and the  $NH_4^+$  plus  $nss-K^+$  molar concentration were usually between 1:1 and 2:1 (Fig. S1b), suggesting that  $nss-SO_4^{2-}$  originated from ammonium sulfate, ammonium bisulfate, and ammonium potassium rather than from sulfuric acid.

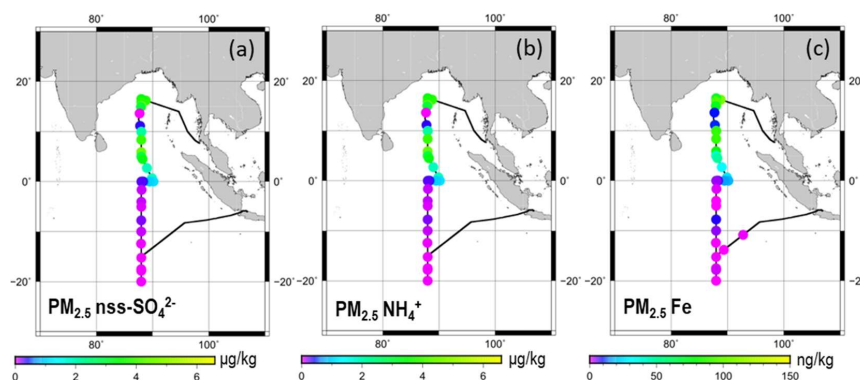


**Figure 2: Horizontal variation of mass concentrations of (a)  $nss-SO_4^{2-}$ , (b)  $NH_4^+$ , and (c) Fe in  $PM_{2.5}$ . Each sample was collected continuously 12 h or 24 h under controlling by wind sector. Data are as shown at averaged locations for latitude and longitude during the sampling period.**



240 **Table 2: Average, 25th percentile and 75th percentile values of PM<sub>2.5</sub> ion concentration (µg/m<sup>3</sup>) at 87–90°E**

	0–16°N			0–20°S		
	average	25th percentile	75th percentile	average	25th percentile	75th percentile
Cl <sup>-</sup>	0.05	0.02	0.04	0.21	0.03	0.30
NO <sub>3</sub> <sup>-</sup>	0.07	0.04	0.09	0.06	0.04	0.08
SO <sub>4</sub> <sup>2-</sup>	13.07	8.32	19.10	1.50	0.48	1.67
Na <sup>+</sup>	0.23	0.19	0.27	0.21	0.08	0.35
NH <sub>4</sub> <sup>+</sup>	3.74	2.24	4.87	0.31	0.03	0.35
K <sup>+</sup>	0.53	0.19	0.78	0.05	0.01	0.07
Mg <sup>2+</sup>	0.04	0.03	0.05	0.03	0.02	0.04
Ca <sup>2+</sup>	0.07	0.04	0.09	0.04	0.03	0.06
nssSO <sub>4</sub> <sup>2-</sup>	13.01	8.25	19.03	1.45	0.40	1.63
nssK <sup>+</sup>	0.52	0.19	0.77	0.04	0.00	0.06
nssCa <sup>2+</sup>	0.06	0.04	0.08	0.03	0.02	0.05

**Table 3: Average, 25th percentile and 75th percentile values of PM<sub>2.5</sub> metal concentration (ng/m<sup>3</sup>) at 87–90°E**

	0–16°N			0–20°S		
	average	25th percentile	75th percentile	average	25th percentile	75th percentile
Na	363.0	274.0	446.0	265.4	86.3	416.8
Al	141.0	57.0	164.0	15.7	0.0	31.8
K	526.8	194.0	550.0	46.1	8.6	69.7
Ca	44.1	20.6	50.2	9.4	5.5	14.7
Ti	5.9	2.3	7.3	0.3	0.0	0.6
V	1.8	0.8	2.3	0.5	0.0	0.8
Fe	78.9	31.4	101.0	5.1	0.1	8.0
Ni	0.8	0.4	1.0	0.1	0.0	0.2
Zn	78.9	32.6	84.5	3.8	0.0	4.2



245 Among metals measured using ICP-MS, the Na and K mass concentrations were high (71–1280 ng m<sup>-3</sup> and 6–  
1210 ng m<sup>-3</sup>, respectively). The Fe concentrations were high (31–162 ng m<sup>-3</sup>) north of the equator, but low (<22  
ng m<sup>-3</sup>) south of the equator. The Fe mass concentrations were well correlated positively with nss-K<sup>+</sup> ( $R^2=0.95$ ),  
nss-SO<sub>4</sub><sup>2-</sup> ( $R^2=0.93$ ), and Ca ( $R^2=0.90$ ) mass concentrations (Fig. S2). The concentrations of V and Ni, which  
originate from heavy oil combustion by ships, were correlated well ( $R^2$  of 0.96). However, their correlations  
250 with Fe concentration ( $R^2$  values of 0.69 and 0.83, respectively) were weaker than the correlation between V  
and Ni and the correlations of Fe found with nss-K<sup>+</sup>, nss-SO<sub>4</sub><sup>2-</sup>, and Ca. These results suggest that a large fraction  
of the observed Fe had been transported from around the continental atmosphere with dust, nss-K<sup>+</sup>, and nss-  
SO<sub>4</sub><sup>2-</sup>. However, the good correlation with continental elements implies that Fe was transported together with  
the continental air mass, but does not imply that emission sources for each element are the same. Therefore,  
255 details of the composition and morphological features of individual Fe-containing particles were investigated  
as described in the following sections.

### 3.2 Individual particle features and co-existing states with Fe of sulfate and soot

Electron microphotographs of samples #01 and #07 are presented in Fig. 3 as examples. Photographs of all  
samples (#01–07) and number fractions of the morphological types observed in our samples are also shown  
260 respectively as Figs. S3 and S4 of Supplemental Materials. The morphological types were classified based on a  
report by Ueda et al. (2016) and features of particles on the samples. For samples #01–06, many particles in all  
samples had a rounded shape (ball) or were clustered into ball shapes (cluster), such as the blue and white  
arrowed particles of sample #01 of Fig. 3. Dome-shaped particles have less height to area (dome). Chain  
aggregation of small globules (ca. 30 nm) is regarded as a particle composed mainly of soot (soot), although  
265 they were a small fraction. For sample #07, some particles constructed of cubic parts having high contrast to an  
electron beam were also found. They can usually be regarded as sea salt (SS)-shaped.

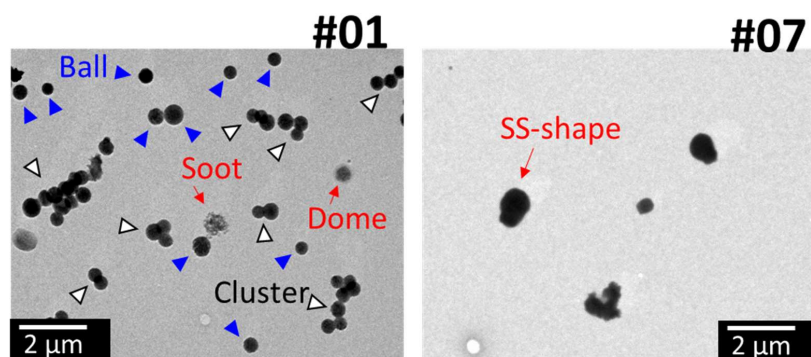
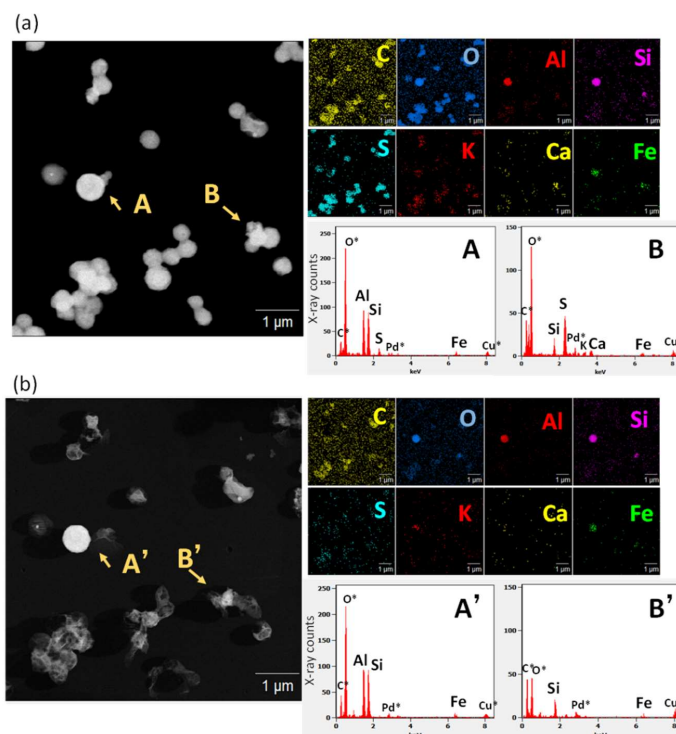


**Figure 3: Electron micrographs for samples #01 and #07. Blue arrowed particles are ball-like shaped particles. White arrowed particles are clusters of balls. Red arrows indicate soot, dome-shaped, and sea-salt (SS)-shaped particles.**

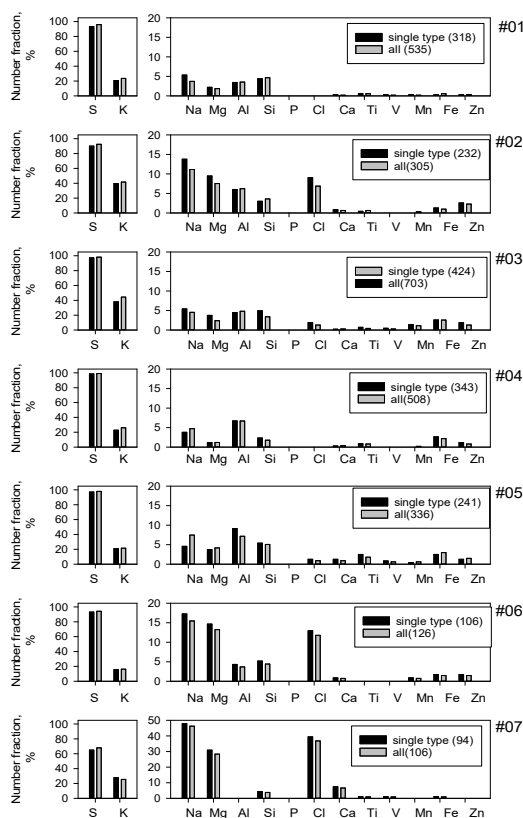
270 Figure 4a shows a STEM image and EDS mapping of C, O, Al, Si, S, K, Ca, and Fe of an area of sample #03  
and examples of the X-ray count spectrum for each particle. Ball-like and clustered particles were composed  
mainly of S, C, and O, indicating sulfate with organics. Also, K signals in the particles were often found at the  
same position as the detected S signal. Number fractions of particles detecting each element are depicted in Fig.  
5. Also, S was detected from >92% of all particles for samples collected north of the equator. K was detected  
275 from 16–44% particles. For other elements, particles containing sea salt (Na, Mg and Cl) were often detected  
(3–48% of all particles). Also, Al and Si were detected in about 5% of particles collected north of the equator.  
Findings show that Fe was detected in 1–4% of all particles.



280

**Figure 4:** STEM image and an elemental map of sample #03 for the same region (a) before and (b) after water dialysis and extracted X-ray count spectrum for arrowed particles A and B and for the same region after water dialysis (A' and B'). Asterisk (\*) elements represent elements included in the background area without particles.





285

**Figure 5: Number fractions of element-containing particles. Single type is particles except cluster shaped particles. Bracketed numbers in the legend are analyzed particles.**

As shown by particles A and B in Fig. 4a, Fe signals were often found from a partial area with attached or coated sulfate. For this study, metal-congested areas containing Fe are designated as Fe-containing parts, to distinguish  
 290 a term from whole particles (Fe-containing particles) such as particles with a co-existing Fe-containing part and sulfate. From some Fe-containing parts, Si, Al and/or Ca were also detected. Compositions of Fe-containing particles and types of Fe-containing parts are detailed in the next section. Figure 4b shows a STEM image, EDS



mapping, and X-ray count spectra after water dialysis for the same area as that shown in Fig. 4a. A large part composed of S and K disappeared with dissolution by water dialysis, suggesting that they have hygroscopicity.

295 However, many parts composed of Si, Al, Fe or C remained on film.

Co-existing Fe-containing parts and sulfate were found from TEM samples. Such particles are probably formed with secondary formation or coagulation of sulfate with an Fe-containing particle. Good correlation between Fe and  $\text{nss-SO}_4^{2-}$ , as explained in Sect. 3.1, also suggests that a large mass of Fe was transported to the ocean with sulfate particles and their precursor gases. Relations of sulfate particle shapes on samples to their acidity have

300 been reported from some earlier microscopic studies as explained hereinafter. Acidic sulfate particles such as sulfuric acid ( $\text{H}_2\text{SO}_4$ ) and bisulfate ( $\text{NH}_4\text{HSO}_4$ ) are usually found as droplets having a satellite structure because of their property of retaining water even if they were collected after diffusion drying (Waller et al., 1963; Frank and Lodge, 1967; Gras and Ayers, 1979; Bigg, 1980; Ferek et al., 1983; Ueda et al., 2011b). By contrast, particles composed mainly of ammonium sulfate collected after passing the diffusion dryer have been found as

305 ball-like, rectangular, regular shapes or clusters (Ueda et al., 2011b; Ueda, 2021). Most particles on samples examined for this study, have a ball-like shape or a cluster. This result indicates that sulfates in the particles were more closely related to neutralized sulfate such as ammonium sulfate than to sulfuric acid, which also corresponds with the result found for  $\text{PM}_{2.5}$ , as shown in Sect. 3.1. Particles composed mainly of ammonium sulfate can be present as solid or liquid under their deliquescence humidity, according to atmospheric humidity

310 experience. In addition, solid ammonium sulfate particles tend to change to rectangular regular shapes when experiencing a metastable humidity condition (Ueda, 2021). However, rectangular particles were rarely observed in this study, although the atmospheric relative humidity (60–81%RH) at the sampling time (Table 1) is usually a metastable condition of ammonium sulfate (35–80%RH). Therefore, sulfate particles in our samples presumably existed as droplet particles in the atmosphere.

315 Based on reports of measurements of single soot mass analysis by Corbin et al. (2018), much soot originating from combustion of heavy fuel oil in ship engines can contain Fe addition to V, Na, and Pb. Some soot particles



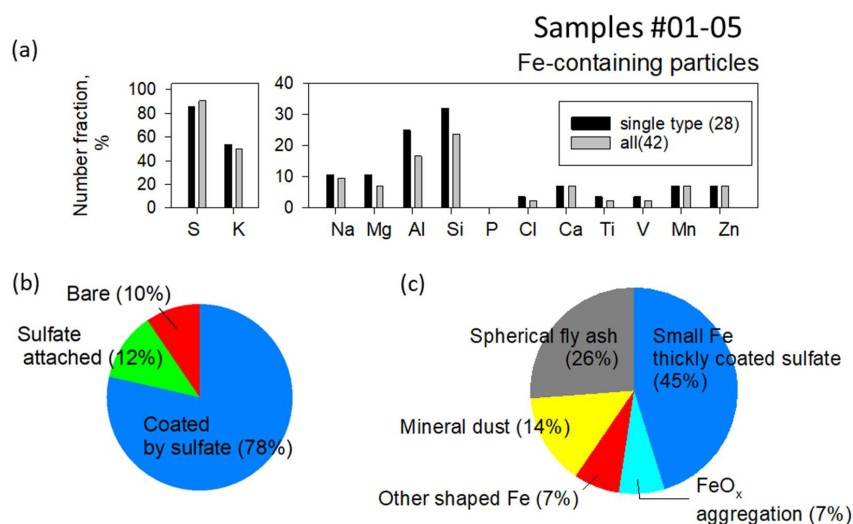
that are less-coated by sulfate were also found from our samples. However, metals including Fe were not detected from less-coated soot particles in this study, as shown in Fig. S5. As reasons for the presence of less-coated soot over the remote ocean, it might be true that hydrophobic or less-coated soot preferentially survives in the atmosphere after transport (Ueda et al., 2018; Kompalli et al., 2021; Ueda et al., 2022) in addition to local ship's exhaust. For our PM<sub>2.5</sub> result, as explained in Sect. 3.1, Fe was somewhat correlated with V, although the correlation was weaker than that between V and Ni, or those between Fe and either nss-SO<sub>4</sub><sup>2-</sup>, nss-K<sup>+</sup> or Ca. Some Fe might have originated in the ship's exhaust, combined with that from transport from continental areas. However, no strong evidence of the ship's exhaust was found from our individual particle observations, including analyses of Fe-containing particles presented hereinafter.

### 3.3 Fe-containing particles: composition and morphological features implying their source

Figures 6a and 6b portray number fractions of particles containing the respective elements and mixing types with sulfate for Fe-containing particles (42 particles) observed in five samples (#01–05) affected by air masses from South Asia. Most Fe-containing particles were mixed with sulfate (Fig. 6b). Actually, S was detected from 90% of Fe-containing particles (Fig. 6a). Also, K was found from half of the Fe-containing particles (Fig. 6a), suggesting that biomass burning affected the Fe-containing particle compositions. However, many K signals were detected from the sulfate coating. Therefore, such K implies secondary formation on Fe-containing parts rather than a source of Fe-containing parts. Both Al and Si were detected from 20% and 30% of Fe-containing particles. Very little V originating from heavy oil combustion of ships was detected from Fe-containing particles. Moreover, Na, Mg, Ca, Mn, and Zn were detected from less than 7–10% of Fe-containing particles. Both Ca and Mg can originate from biomass burning in addition to sea salt and mineral dust. Adachi et al. (2022) reported ash-bearing particles found in biomass burning smoke based on TEM analysis of fine (<2.5 μm) particles. They defined particles containing both Ca and Mg (>5 weight%) as ash-bearing particles. According to them, ash-



340 bearing particles from biomass burning smoke commonly have aggregated shapes with complicated compositions, predominantly calcium with other elements (e.g., C, O, Mg, Al, Si, P, S, and Fe). However, for our study, the Fe-containing particles mixed with both Ca and Mg were only one (2% of Fe-containing particles). In addition, morphological features of Fe-containing particles were less like ash-bearing particles reported by Adachi et al. (2022).



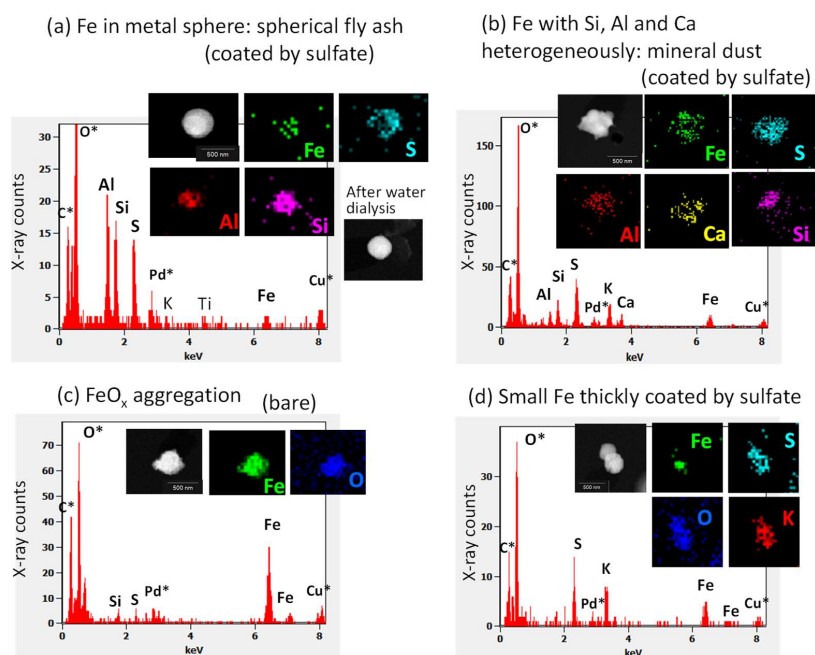
345

**Figure 6: Mixing states and morphological features of Fe-containing particles of samples collected north of the equator. (a) Number fraction of each-element-containing particles in Fe-containing particles. (b) Pie chart of mixing type with sulfate. (c) Pie chart of Fe-containing part types based on elements and morphology. Section 3.3 presents classification methods of Fe-containing part types. Single type in (a) is particles extracted clustered shaped particles.**

350 As shown in Figs. 4a and 4b, Fe-containing parts had some different morphological types, such as spherical or irregular shapes and homogeneous or heterogeneous mixing with other elements. Such morphological types can be related to their Fe emission source. Based on contrast of STEM images and EDS mapping, we divided Fe-containing parts to three morphological types associated with an emission source (spherical fly ash, mineral



dust,  $\text{FeO}_x$  aggregation) and the other two types (other-shaped Fe and small Fe thickly coated by sulfate).  
 355 Average  $\pm$  standard deviation values of  $\text{Fe}/\text{Pd}$  for each type above were, respectively,  $1.1 \pm 2.2$ ,  $0.18 \pm 0.14$ ,  
 $0.73 \pm 0.81$ ,  $1.7 \pm 0.6$ , and  $0.07 \pm 0.05$ . The number fractions for the morphological types for Fe-containing  
 particles are presented in Fig. 6c. For sample #03, the morphology after water dialysis was also referenced. In  
 addition, examples of STEM images, the elemental map, and X-ray spectra for typical Fe-containing particles  
 are portrayed in Fig. 7. Details for the respective morphological types are explained later in Sects. 3.3.1–3.3.4.



360

**Figure 7: Examples of STEM images, elemental maps, and X-ray count spectra of typical Fe-containing particles. (a) Example of particle having a Fe-containing part in metal sphere (spherical fly ash). The metal sphere part of this particle is coated by sulfate. (b) Example of Fe-containing particle co-existing with Si, Al or Ca heterogeneously (mineral dust). The Fe, Si, Al, and Ca part of this particle is coated by sulfate. (c) Example of  $\text{FeO}_x$  aggregation particles. (d) Example of particle having small Fe-containing part thickly coated by sulfate. Asterisk (\*) elements in the X-ray count spectrum represent elements contained in the background area without particles.**

365



### 3.3.1 Fe in metal sphere (spherical fly ash)

As shown for particle A in Fig. 4 and for the particle in Fig. 7a, Fe-containing spheres with Al and/or Si were found in nine particles (21% of Fe-containing particles) from samples #03 and #04, affected by air masses from the eastern coast of India (Table S1 and Fig. 1b). In addition, Fe spheres without Al or Si were found as two particles (5% of Fe-containing particles) from sample #05, affected by air masses from the Maldives. All particles containing metal spheres of both types co-existed with sulfate. In the STEM image, such metal spheres have high contrast compared to sulfate. Such spheres remained as a residue after water dialysis. Spherical shapes of metals indicate that they were formed through evaporation at high temperatures and subsequent rapid condensation. Moreover, the shape coincides with often encountered features of fly ash particles originating from coal combustion at power plants (e.g. Fisher et al., 1978; Yao et al., 2015; Umo et al., 2019). For this study, metal spheres composed mainly of Fe, Si or Al in our atmospheric aerosol samples are designated as spherical fly ash to distinguish them from fly ash related to emission sources that are not classified using morphology. In coal, Fe generally exists in two forms: as pyrite or aluminosilicate (Tomeczek and Palugniok, 2002). Aluminosilicate-Fe such as kaolinite and illite generally undergoes high-temperature melting and fragmentation, leading to formation as fly ash (Rathod et al., 2020). Although low-temperature combustion processes such as residential uses might not engender Fe volatilization (Flagan and Seinfeld, 2012), power plants can emit fly ash efficiently (Rathod et al., 2020). Although the mass concentration peak of fly ash emitted from power plants is super-micrometric (1–10  $\mu\text{m}$ ), submicrometer fly ash particles are also emitted together. They have been observed and described in the literature (Markowski and Filby, 1985; Liu et al., 2018; Umo et al., 2019).

### 3.3.2 Fe co-existing with Al, Si or Ca heterogeneously (mineral dust)

As shown for particle B in Fig. 4 and for the particle in Fig. 7b, some non-spherical parts containing Fe, Si, and Al were also found. Unlike the Fe-containing sphere parts explained earlier, Ca was usually detected from such non-spherical Fe-containing parts. Additionally, they have some domains of different concentrations of Fe, Al,



390 Si, and Ca. The Fe, Al, Si and Ca are main elements of silicate minerals. Mineral dust is usually composed of  
some different mineral species domains (Conny, 2013; Jeong and Nousiainen, 2014; Jeong et al., 2014 and  
2016; Conny et al., 2019; Ueda et al. 2020). Therefore, heterogeneous structures such as Fe, Al, Si and Ca imply  
that they are mineral dusts without any origin related to combustion. Such Fe-containing parts regarded as  
mineral dust were found in six particles (14% of Fe-containing particles) in samples #01, 03, 04, and 05 (Table  
395 S1). Most particles of this type (five particles) co-existed with sulfate. Based on water dialysis of sample #03,  
Ca in particle B in Fig. 4a dissolved with water dialysis, as shown in Fig. 4b. Although calcite in dust is poorly  
soluble, chemical transformation from them into calcium sulfate or calcium nitrate with atmospheric aging can  
alter their solubility (Okada et al., 1990, 2005; Zhang and Iwasaka, 1999; Matsuki et al. 2005).

### 3.3.3 FeO<sub>x</sub> aggregation

400 Some aggregate components comprising Fe and O without other metals were found as shown for a particle in  
Fig. 7c. They are regarded as being FeO<sub>x</sub>, such as magnetite and illite. Similar aggregated FeO<sub>x</sub> nanoparticles  
have often been reported from several observational studies of urban atmospheres using electron microscopy  
methods (Hu et al., 2015; Adachi et al., 2016; Ohata et al., 2018), roadside environments (Sanderson et al.,  
2016), and polluted remote seas (Li et al., 2017). Aggregated FeO<sub>x</sub> co-existing with soot was also found at urban  
405 sites (Ohata et al., 2018; Ueda et al., 2022). From this study, FeO<sub>x</sub> aggregation (classified as FeO<sub>x</sub> aggregation)  
was found as without a C-rich part from three particles (7% of Fe-containing particles) in samples #02, 03, and  
04, affected by air masses from India (Table S1 and Fig. 1). Two FeO<sub>x</sub> aggregations co-existing with sulfate  
were found. As explained in Sect. 3.2, soot-containing metals were also minor. The FeO<sub>x</sub> can be emitted from  
blast furnaces at Fe-working facilities (Machemer, 2004) and as exhaust from motor vehicles (Kukutschová et  
410 al., 2011; Liati et al., 2015). However, considering FeO<sub>x</sub> without soot, FeO<sub>x</sub> aggregations examined in this study  
might have originated mainly from the former source.



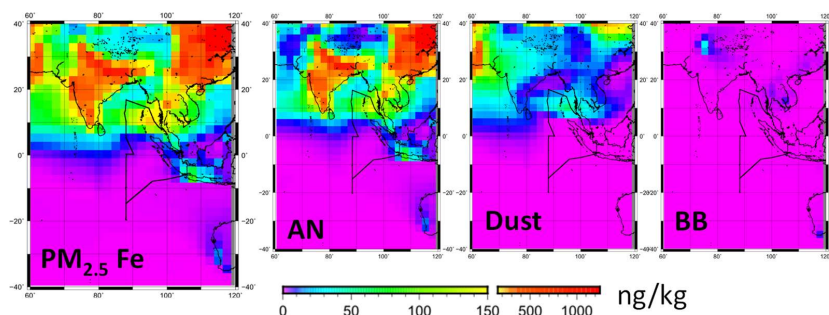
### 3.3.4 Other-shaped Fe and small Fe thickly coated by sulfate

For Fe-containing parts of three particles (7% of Fe-containing particles), different shapes were found in terms of the features above: spherical fly ash, mineral dust, and FeO<sub>x</sub> aggregation. They were classified as other-shaped Fe. Of them, two particles were without sulfate. For the other 19 Fe-containing particles, discriminating the shapes of Fe-containing parts was difficult because such parts were too small compared to the sulfate coating, as illustrated in Fig. 7d. Such Fe-containing particles were classified as small Fe thickly coated by sulfate separately from other shaped Fe. The number fraction was 45% of the Fe-containing particles. However, the *Fe/Pd* values ( $0.07 \pm 0.05$ ) from such small Fe were usually less than those of the other types.

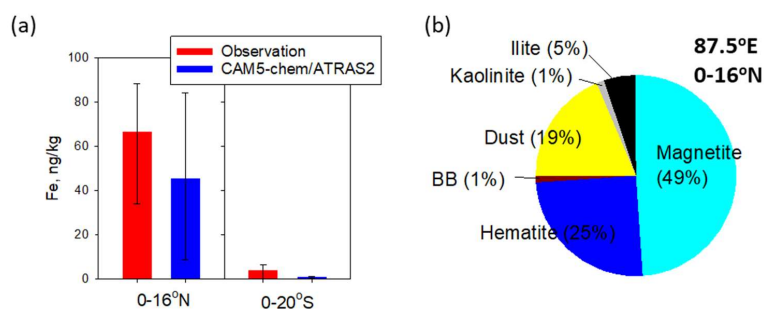
### 3.4 Fe simulation for each source by the global model

To elucidate the origins of Fe and the model performance, Fe simulation results using the CAM5-ATRAS model were compared with observation results. Figure 8 shows the monthly mean simulated mass concentrations in PM<sub>2.5</sub> for total Fe and Fe from each source at the surface. The color scale of 0–150 ng/kg is the same as that presented for Fig. 2c. Averages of the total Fe mass concentrations for areas north and south of the equator along the ship tracks (0–16°N and 0–20°S at 87.5°E) are shown in Fig. 9a with the observed values. Although the simulated Fe mass tends to be lower than the observed Fe mass, the model simulations well reproduce the contrast of Fe mass between the north (high concentration) and south (low concentration) during the cruise.





430 **Figure 8:** Spatial distribution of total, anthropogenic (AN), mineral dust (Dust), and biomass burning (BB) iron concentration of  $PM_{2.5}$  simulated by CAM5-chem/ATRAS2 model. Values are monthly averaged mass concentrations for November 2018.



435 **Figure 9:**  $PM_{2.5}$  Fe mass concentration simulated by CAM5-chem/ATRAS2. (a) Averaged  $PM_{2.5}$  Fe simulated value for  $87.5^{\circ}E$  and observed  $PM_{2.5}$  Fe of  $87-90^{\circ}E$  during the KH18-06 cruise. The lower and upper error bars respectively stand for the 25th and 75th percentiles. (b) Pie chart of averaged mass fraction simulated  $PM_{2.5}$  Fe for each Fe species of  $0-15^{\circ}N$  at  $87.5^{\circ}E$ . Simulated values are monthly averaged mass concentrations for November 2018.

The CAM5-ATRAS results show that the anthropogenic Fe was dominant in  $PM_{2.5}$  Fe concentration within the area shown in Fig. 8. The averaged mass fraction of each Fe source/mineral type in the model for  $0-15^{\circ}N$  at  $87.5^{\circ}E$  estimated are depicted in Fig. 9b. The anthropogenic Fe (magnetite, hematite, illite, and kaolinite), dust  
 440 Fe and biomass-burning Fe were, respectively, 80%, 19%, and 1% of the mass of  $PM_{2.5}$  Fe. Especially, anthropogenic Fe around India has a high concentration in Fig. 8. The anthropogenic activity of the area might have affected Fe concentrations over the Indian Ocean.



The anthropogenic Fe was mostly (74% in mass of  $PM_{2.5}$  Fe) estimated as  $FeO_x$  (magnetite and hematite). The mass fraction of anthropogenic aluminosilicates Fe (illite and kaolinite), which derive mainly from coal  
445 combustion, was only 6% in the model. These simulation results might underestimate the fraction of aluminosilicate Fe and overestimate the fraction of  $FeO_x$ , compared to the TEM results. In the TEM samples, spherical fly ash having sufficient  $Fe/Pd$  values were often found (26% of Fe-containing particles) as shown in Fig. 6. Also, most of them (8 in 11 spherical fly ash particles) contained Al and/or Si. Mineralogy of Fe from coal combustion in emission inventory by Rathod et al. (2020), which is used in our model, was estimated from  
450 reference to mineralogical measurements of bulk samples using Mossbauer spectrometry or the X-ray absorption near-edge structure. Although the mineralogical transformation from fuels to by-product can be affected by fuels and combustion temperatures, the Fe contents estimated from mineralogical measurements of coal fly ash at power plants tend to comprise both oxides (such as magnetite and hematite) and clay (such as kaolinite and illite) (Hinckley et al., 1980; Szumiata et al., 2015; Waanders et al., 2003; Oakes et al., 2012;  
455 Rathod et al., 2020). However, even if Fe in spherical fly ash in our TEM samples were assumed to be composed of aluminosilicates and equivalent  $FeO_x$ , the mass fraction of aluminosilicates Fe inferred from TEM results would be larger than 13%, which is higher than our model simulated results. The chemical composition and size-mass distribution of coal fly ash particles at the source can be affected by multiple factors such as the fossil fuel composition and combustor (Markowski and Filby, 1985; Liu et al., 2018). Their lack of clarity can also  
460 affect the uncertainty of simulation for the emission of Fe originated in coal combustion and the transport according to the particle size.

### 3.5 Water solubility of Fe

Figure 10 portrays the relation between  $Fe/Pd$  before and after water dialysis and  $f_{WSFe}$  for Fe-containing particles (14 particles) for sample #03. The symbols were made according to the composition and shape of  
465 residues after water dialysis. For particles containing metal sphere residues regarded as fly ash, the values of



Fe/Pd after water dialysis of Figs. 10a and 10b correspond well to the values before water dialysis at a 1:1 ratio. Because Pd mass after water dialysis can be regarded as equal to that before water dialysis, such a 1:1 relation indicates that the Fe in spherical fly ash was almost insoluble in water. For particles aside from metal spheres containing residues, the detected values of  $Fe/Pd$  decreased, suggesting that some Fe were soluble in water. The averages of  $f_{WSFe}$  were 48%, 6%, 58%, and 65%, respectively, for all Fe-containing particles of spherical fly ash, mineral dust, and Fe-containing particles, except spherical fly ash (Fig. 10c).

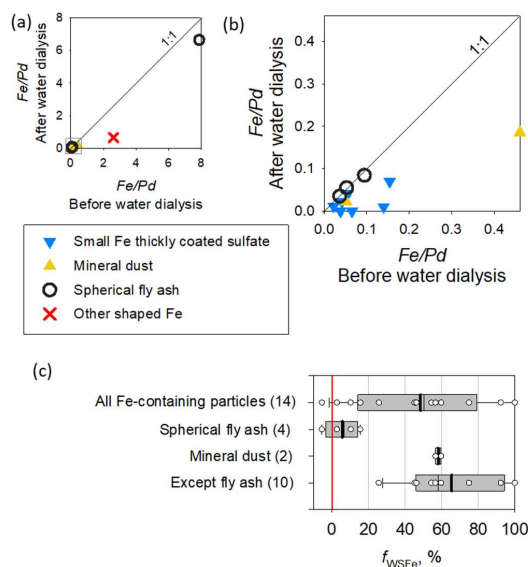


**Figure 10: Relations of water-soluble and water-insoluble Fe in individual Fe-containing particles on sample #03. (a) Scatter plot of Fe weight normalized Pd before and after water dialysis. Pd is a coating material in alloy for shadowing to samples. (b) Enlarged graph of the light-gray squared area of (a). (c) Box plot of water-soluble Fe fraction ( $f_{WSFe}$ ). The lower boundary of the box shows the 25th percentile. The line within the box represents the median. The upper boundary of the box stands for the 75th percentile. Whiskers above and below the box respectively show the 90th and 10th percentiles. White circles show values for the respective particles.**



Some measurement studies for bulk aerosol samples have reported fractions of water-soluble Fe in all Fe  
480 (Kumar and Sarin, 2010; Baker et al., 2013; Ingall et al., 2018). After Kumar and Sarin (2010) also measured  
Fe in PM<sub>2.5</sub> at a high-altitude site in a semi-arid region of western India, they reported fractions of water-soluble  
Fe as 0.06–16.1%. Ingall et al. (2018) measured the water solubility of total Fe in bulk aerosol samples taken  
from multiple locations in the Southern and Atlantic oceans, Noida (India), Bermuda, and the eastern  
Mediterranean (Crete). Their fractions of water-soluble Fe were low (<5%) under samples influenced by  
485 Saharan dust, but the fractions for samples of Noida (3–20%) and samples influenced from Europe were high  
(17–35%), indicating an anthropogenic contribution of soluble Fe. From measurements taken of the remote  
ocean, Baker et al. (2013) reported Fe solubility 2.4–9.1% of aerosol collected in the Atlantic Ocean during  
research cruises. Compared to Fe solubility by the studies described above, the water-soluble Fe fraction for  
individual Fe-containing particles in this study tended to be estimated as higher. This finding might be attributed  
490 to the fact that our analyzed samples were smaller particles (0.3–0.8 μm samples stage diameter), with a greater  
surface relative to the particle mass, and aged particles collected over the remote ocean, as explained below.  
The values of  $f_{\text{WSFe}}$  in this study were 20–100% in Fe-containing particles, except spherical fly ash. Among Fe-  
containing minerals, the fraction of water-soluble Fe in FeO<sub>x</sub> (magnetite, goethite and hematite) and clays (such  
as kaolinite and illite) are very low (respectively, <0.01% and 1.5–4%), but that of ferrous and ferric sulfate is  
495 higher (50–90%) (Desboeufs et al., 2005; Schroth et al., 2009; Journet et al., 2008; Rathod et al., 2020). The Fe  
solubilities for many Fe-containing particles in this study were comparable to those of ferrous and ferric sulfate.  
Our earlier study often found non/less-sulfate-coated FeO<sub>x</sub> in aerosol samples collected in urban Tokyo, for  
which we applied the same analysis (Ueda et al., 2022). However, few decreases of Fe with water dialysis were  
found. The difference of Fe solubility found from this urban study might be attributed to atmospheric aging  
500 processes by coating of secondary aerosol materials and Fe oxidation during transport. Some experimentation  
and simulation studies have indicated that Fe in minerals composed of Fe oxide and clays can be oxidized and  
enhanced in acidic liquid phase such as aerosol droplets and clouds (Shi et al., 2009 and 2015; Chen et al., 2012).



For the present study, most of the observed Fe-containing particles co-existing with sulfate were regarded as droplets in the atmosphere. Therefore, Fe in particles might have oxidized in liquid droplet particles in the atmosphere, after which they were later collected as water-soluble Fe, such as Fe sulfate. For Fe-containing particles in this study, the number fraction of FeO<sub>x</sub> aggregation was less, whereas that of categorized particles to small Fe thickly coated by sulfate was higher. This result might also be affected somewhat by the loss of the water-insoluble Fe shape by change to water-soluble Fe.

All water insoluble residues in Fe-containing particles of  $f_{\text{WSFe}} < 15\%$  were spherical fly ash. Although all of them co-existed with sulfate, water dialysis results indicated that the water insolubility of Fe in them was retained. Our observed insoluble sphere residues imply structural and morphological features as reasons for the insolubility of the Fe contained in aged fly ash particles. Spherical particles have the minimum surface area. In addition, the Fe is distributed in particles with other insoluble materials composed of Si and Al in the sphere. This distribution would physically block the oxidation and dissolution of Fe. However, results of several studies have suggested that Fe in similar spherical fly ash particles can dissolve in acidic particles (Chen et al., 2012; Li et al., 2017). Li et al. (2017) observed similar submicrometer Fe-rich spheres coated by sulfate in samples collected over the yellow sea affected by the East Asian continental outflow. They analyzed sulfate-rich particles containing Fe-rich parts using nanoscale secondary ion mass spectrometry and elemental mapping with STEM, and reported the presence of dispersed FeS<sup>+</sup> (Fe sulfate) around FeO<sup>+</sup> (Fe oxide)-rich part. They concluded that such Fe sulfate was formed from Fe dissolution of fly ash in an acidic aqueous phase because no other atmospheric source of Fe sulfate or process leads to its formation. Using bulk samples of coal fly ash composed mainly of spherical particles, Chen et al. (2012) also investigated Fe dissolution. Their experiments demonstrated that Fe in coal fly ash can dissolve in H<sub>2</sub>SO<sub>4</sub> acidic aqueous solutions of pH 1 and 2. These earlier reported study results suggest that some Fe in fly ash can exist as water-soluble Fe in sulfuric acid particles. However, results of our experiments indicated that soluble Fe in spherical fly ash was considerably less or nonexistent compared to insoluble Fe. From the present study, as shown in Sect. 3.2, sulfate particles were



found as particles neutralized, such as by ammonium. Such atmospheric conditions observed in the present study might not have decreased pH sufficiently to enhance the Fe solubility of fly ash.

Our observation results of TEM samples suggest fly ash as an important component of fine Fe-containing  
530 particles. In addition, water dialysis results suggest that Fe in aged particles over the remote ocean tend to exist as partly or mostly water soluble, whereas Fe in spherical fly ash can maintain water-insolubility. Model simulations have led to estimates that  $\text{FeO}_x$  was a major component in  $\text{PM}_{2.5}$  Fe of this area and that Fe from anthropogenic aluminosilicates from sources such as coal combustion was minor. Underestimation of the mass fraction of Fe keeping water insoluble during atmospheric transport can be a factor affecting the estimation error  
535 of water-soluble Fe deposition. In addition, although Fe mineralogy is often used for the simulation of solubility of anthropogenic Fe in percent in some models, the spherical shape of fly ash particles and the results of water dialysis imply that Fe solubility and the change in the atmosphere depend not only on the mineralogical but also the morphological and structural features of fly ash originating from emission processes. The presence of fly ash in fine aerosols should be noted for model simulation of water-soluble Fe and estimations based on size-  
540 segregated samples of Fe concentrations.

#### 4 Summary and Conclusions

To elucidate the mixing states and water solubility of Fe-containing particles in remote marine areas, we conducted ship-borne aerosol observations over the Indian Ocean during the R/V Hakuho Maru cruise. After  
545 TEM samples for individual particle analysis were obtained, they were also analyzed using EDS and water dialysis. Most of the particles were composed mainly of sulfate neutralized by ammonium or potassium: the particle number fraction, 0.6–3.0%, of particles on a sample stage of 0.3–0.8  $\mu\text{m}$  diameter contained Fe. They mostly co-existed with sulfate.



Backward air mass trajectory analyses suggest that air masses south of the equator were transported from  
550 southern India. Both the correlations of the respective elements measured using chemical analysis for bulk  $PM_{2.5}$   
samples and the absence of V and soot for individual Fe-containing particles implied that the Fe in particles was  
transported mainly from around the continent rather than from ship exhaust. The Fe in particles was found to  
be 26% metal spheres, often co-existing with Al or Si, regarded as fly ash, 14% as irregularly shaped  
heterogeneously co-existing with Si, Al or Ca, regarded as mineral dust, and 7% as  $FeO_x$  aggregations.

555 Global model simulations using a recent emissions inventory mostly reproduced the observed  $PM_{2.5}$  Fe  
concentrations in the north and south during the cruise. The model simulations suggested that  $PM_{2.5}$  Fe over the  
observation site was influenced strongly by anthropogenic Fe emissions around India. In contrast, compared  
with the morphological features of observed Fe, the simulations tend to overestimate the fractions of  
anthropogenic  $FeO_x$  and to underestimate the fraction of Fe in aluminosilicates originating from coal  
560 combustion.

Water-dialysis analysis for a TEM sample indicated that about half of the Fe in Fe-containing particles was  
soluble in water. However, Fe in spherical fly ash particles was almost insoluble in water even when co-existing  
with sulfate. Dissolution and oxidation of Fe in spherical fly ash might have been blocked by the small surface  
of the sphere and the structure of Fe-dispersion in other insoluble aluminosilicates.

565 Our results obtained from shipboard observations and individual fine aerosol analysis indicate that Fe of various  
types, such as fly ash,  $FeO_x$ , and mineral dust, coexist with sulfate over the remote Indian Ocean, and indicate  
that their solubilities differ among types. Although the model simulations show good agreement with the  
observed Fe mass concentrations, we also find a marked difference in the mass fractions of mineral sources of  
model simulations compared to observed Fe types. Earlier studies have indicated that anthropogenic fine Fe  
570 tends to be composed mainly of  $FeO_x$ , with increased solubility occurring along with aging. However, our results  
suggest that Fe in spherical fly ash can stand out in fine aerosols over the remote ocean and maintain water  
insolubility. For accurate estimation of the effects of atmospheric Fe on marine biogeochemical activity, more



proper attention must be devoted to morphological and mineral types of Fe depending on the source, especially to insoluble Fe in fly ash.

575

### **Acknowledgments**

We are indebted to staff members of the Hakuho Maru for assisting our work on board and Prof. K. Osada of Nagoya University for support and technical advice. We also extend my gratitude for technical support from the High Voltage Electron Microscope Laboratory of Nagoya University. We gratefully acknowledge the  
580 NOAA Air Resources Laboratory (ARL) for providing the HYSPLIT transport model (<http://www.arl.noaa.gov/ready.html>). This study was supported by the Ministry of Education, Culture, Sports, Science, and Technology and the Japan Society for the Promotion of Science (MEXT/JSPS) KAKENHI Grant Numbers 18H03369, 18J40204, 19K20438, 22K18023, JP19H04253, JP19H05699, JP19KK0265, JP20H00196, JP20H00638, JP21K12230, JP22H03722, and JP22F22092, MEXT Arctic Challenge for  
585 Sustainability phase II (ArCS-II; JPMXD1420318865) projects, and the Environment Research and Technology Development Fund 2–2003 (JPMEERF20202003) of the Environmental Restoration and Conservation Agency. M.L. acknowledges the support of JSPS Postdoctoral Fellowships for Research in Japan (Standard).

### **Data availability**

Back-trajectory data were calculated from the NOAA HYSPLIT model  
590 (<https://www.ready.noaa.gov/HYSPLIT.php>, last access: 08 March 2018). Other data will be provided upon request.





### Author contributions

SU, YI and FT designed the study. SU analyzed TEM samples and wrote the paper. YI worked on board for aerosol sampling and measurement. YI and FT contributed to chemical analyses of PM<sub>2.5</sub> samples. HM and ML  
595 conducted numerical model simulations using CAM5-ATRAS.

### Competing interests

The authors declare that they have no conflict of interest.

### References

- Adachi, K., Moteki, N., Kondo, Y. and Igarashi, Y.: Mixing states of light-absorbing particles measured using  
600 a transmission electron microscope and a single-particle soot photometer in Tokyo, Japan, *J. Geophys. Res. Atmos.*, 121, 9153–9164, doi:10.1002/2016JD025153, 2016.
- Andreae, M. O.: Soot carbon and excess fine potassium: long-range transport of combustion-derived aerosols, *Science*, 220, 11481151, doi: 10.1126/science.220.4602.1148, 1983.
- Baker, A. R., Adams, C., Bell, T. G., Jickells, T. D., and Ganzeveld, L.: Estimation of atmospheric nutrient  
605 inputs to the Atlantic Ocean from 50°N to 50°S based on large-scale field sampling: Iron and other dust-associated elements, *Global Biogeochem. Cycles*, 27, 755–767, doi:10.1002/gbc.20062, 2013.
- Bigg, E. K.: Comparison of aerosol at four baseline atmospheric monitoring stations, *J. Appl. Meteorol.*, 19, 521–533, doi:10.1175/1520-0450(1980)019<0521:COAafb>2.0.CO;2, 1980.
- Bradley, W. F. and Grim, R. E.: High temperature thermal effects of clay and related materials, *American  
610 Mineralogist, Journal of Earth and Planetary Materials*, 36(3–4), 182–201, 1951.
- Chen, H., Laskin, A., Baltrusaitis, J., Gorski, C. A., Scherer, M. M., and Grassian, V. H.: Coal fly ash as a source of iron in atmospheric dust, *Environ. Sci. Technol.*, 46, 2112–2120, doi:10.1021/Es204102f, 2012.



- Chen, Y. Wild, O., Conibear, L., Ran, L., He, J. Wang, L., and Wang, Y.: Local characteristics of and exposure to fine particulate matter (PM<sub>2.5</sub>) in four Indian megacities, *Atmos. Environ.*, X5, 100052, 615 doi:10.1016/j.aeaoa.2019.100052, 2020.
- Chuang, P. Y., Duvall, R. M., Shafer, M. M., and Schauer, J. J.: The origin of water soluble particulate iron in the Asian atmospheric outflow, *Geophys. Res. Lett.*, 32, L07813, doi: 10.1029/2004GL021946, 2005.
- Conny, J. M.: Internal composition of atmospheric dust particles from focused ion-beam scanning electron microscopy, *Environ. Sci. Technol.*, 47, 8575–8581, doi:org/10.1021/es400727x, 2013.
- 620 Conny, J. M., Willis, R. D., and Ortiz-Montalvo, D. L.: Analysis and optical modeling of individual heterogeneous Asian Dust Particles collected at Mauna Loa Observatory, *J. Geophys. Res.–Atmos.*, 124(5), 270–2723, doi:10.1029/2018JD029387, 2019.
- Corbin, J. C., Mensah, A. A., Pieber, S. M., Orasche, J., Michalke, B., Zanatta, M., Czech, H., Massabò, D., Buatier de Mongeot, F., Mennucci, C., El Haddad, I., Kumar, N. K., Stengel, B., Huang, Y., Zimmermann, 625 R., Prévôt, A. S. H., and Gysel, M.: Trace metals in soot and PM<sub>2.5</sub> from heavy-fuel-oil combustion in a marine engine, *Environ. Sci. Technol.*, 52 (11), 6714–6722, doi: 10.1021/acs.est.8b01764, 2018.
- Cwiertny, D. M., Baltrusaitis, J., Hunter, G. J., Laskin, A., Scherer, M. M., and Grassian, V. H.: Characterization and acid-mobilization study of iron-containing mineral dust source materials, *J. Geophys. Res. Atmos.*, 113(D5), doi:10.1029/2007JD009332, 2008.
- 630 de Baar, H. J. W., Boyd, P. W., Coale, K. H., Landry, M. R., Tsuda, A., Assmy, P., Bakker, D. C. E., Bozec, Y., Barber, R. T., Brzezinski, M. A., Buesseler, K. O., Boye, M., Hiscock, W. T., Laan, P., Lancelot, C., Law, C.S., Levasseur, M., Marchetti, A., Millero, F. J., Nishioka, J., Nojiri, Y., Oijen, T., Riebesell, U., Rijkensberg, M. J. A., Saito, H., Takeda, S., Timmermans, K. R., Veldhuis, M. J. W., Waite, A. M., and Wong, C.: Synthesis 635 of iron fertilization experiments: from the Iron Age in the Age of Enlightenment, *Journal of Geophysical Research*, 110, p. C09S16, doi:10.1029/2004JC002601, 2005.



- Desboeufs, K. V., Sofikitis, A., Losno, R., Colin, J. L., and Ausset, P.: Dissolution and solubility of trace metals from natural and anthropogenic aerosol particulate matter, *Chemosphere*, 58(2), 195–203, doi:10.1016/j.chemosphere.2004.02.025, 2005.
- 640 Duce, R. A. and Tindale, N. W.: Atmospheric transport of iron and its deposition in the ocean, *Limnol. Oceanogr.*, 36, 1715–1726, doi: 10.4319/lo.1991.36.8.1715, 1991.
- Ferek, R. J., Lazrus, A. L., and Winchester, J. W.: Electron microscopy of acidic aerosols collected over the northeastern United States, *Atmos. Environ.*, 17, 1545–1561, doi:10.1016/0004-6981(83)90308-6, 1983.
- Fisher, G. L., Prentice, B. A., Silberman, D., Ondov, J. M., Biermann, A. H., Ragaini, R. C., and McFarland, 645 A. R.: Physical and morphological studies of size-classified coal fly ash, *Environ. Sci. Technol.*, 12, 447–451, doi:10.1021/es60140a008, 1978.
- Flagan, R. C. and Seinfeld, J. H.: *Fundamentals of air pollution engineering*. Courier Corporation, 2012.
- Frank, E. R. and Lodge, J. P.: Morphological identification of airborne particles with the electron microscope, *J. Microscope*, 6, 449–456, 1967. Gras, J. L. and Ayers, G. P.: On sizing impacted sulfuric acid aerosol 650 particles, *J. Appl. Meteorol.*, 18, 634–638, doi:10.1175/1520-0450(1979)018<0634:OSISAA>2.0.CO;2, 1979.
- Guieu, C., Bonnet, S., Wagener, T., and Loÿe-Pilot, M.-D.: Biomass burning as a source of dissolved iron to the open ocean? *Geophys. Res. Lett.*, 32, L19608, doi: 0.1029/2005GL022962, 2005.
- Guttikunda, S. K., Goel, R., and Pant, P.: Nature of air pollution, emission sources, and management in the 655 Indian cities, *Atmos. Environ.*, 95, 501–510, doi: 10.1016/j.atmosenv.2014.07.006, 2014.
- Harrison, P. J., Boyd, P. W., Varela, D. E., Takeda, S., Shiimoto, A., and Odate, T.: Comparison of factors controlling phytoplankton productivity in the NE and NW subarctic Pacific gyres, *Prog. Oceanogr.*, 43, 205–234, doi:10.1016/S0079-6611(99)00015-4, 1999.
- Hidemori, T., Nakayama, T., Matsumi, Y., Kinugawa, T., Yabushita, A., Ohashi, M., Miyoshi, T., Irei, S., 660 Takami, A., Kaneyasu, N., Yoshino, A., Suzuki, R., Yumoto, Y., and Hatakeyama, S.: Characteristics of



- atmospheric aerosols containing heavy metals measured on Fukue Island, Japan, *Atmos. Environ.*, 97, 447–455, doi:10.1016/j.atmosenv.2014.05.008, 2014.
- Hinckley, C. C., Smith, G. V., Twardowska, H., Saporoschenko, M., Shiley, R. H., and Griffen, R. A.: Mössbauer studies of iron in Lurgi gasification ashes and power plant fly and bottom ash, *Fuel*, 59(3), 161–665, doi:10.1016/0016-2361(80)90160-X, 1980.
- Hu, Y., Lin, J., Zhang, S., Kong, L., Fu, H., and Chen, J.: Identification of the typical metal particles among haze, fog, and clear episodes in the Beijing atmosphere, *Sci. Total Environ.*, 511, 369–380, doi:10.1016/j.scitotenv.2014.12.071, 2015.
- Ingall, E. D., Feng, Y., Longo, A. F., Lai, B., Shelley, R. U., Landing, W. M., Morton, P. L., Nenes, A., 670 Mihailopoulos, N., Violaki, K., Gao, Y., Sahai, S., and Castorina, E.: Enhanced iron solubility at low pH in global aerosols, *Atmosphere*, 9, 201, doi:10.3390/atmos9050201, 2018.
- Ito, A.: Atmospheric processing of combustion aerosols as a source of bioavailable iron, *Environ. Sci. Technol. Lett.*, 2, 70–75, doi:10.1021/acs.estlett.5b00007, 2015
- Ito, A. and Feng, Y.: Role of dust alkalinity in acid mobilization of iron, *Atmos. Chem. Phys.*, 10, 9237–9250, 675 doi:10.5194/acp-10-9237-2010, 2010.
- Iwamoto, Y., Narita, Y., Tsuda, A., and Uematsu, M.: Single particle analysis of oceanic suspended matter during the SEEDS II iron fertilization experiment, *Marine Chemistry*, 113, 212–218, doi:10.1016/j.marchem.2009.02.002, 2009.
- Iwamoto, Y., Yumimoto, K., Toratani, M., Tsuda, A., Miura, K., Uno, I., and Uematsu, M.: Biogeochemical 680 implications of increased mineral particle concentrations in surface waters of the northwestern North Pacific during an Asian dust event, *Geophys. Res. Lett.*, 38, L01604, doi:10.1029/2010GL045906, 2011.
- Jeong, G. Y., Kim, J. Y., Seo, J., Kim, G. M., Jin, H. C., and Chun, Y.: Long-range transport of giant particles in Asian dust identified by physical, mineralogical, and meteorological analysis, *Atmos. Chem. Phys.*, 14, 505–521, doi:10.5194/acp-14-505-2014, 2014.



- 685 Jeong, G. Y. and Nousiainen, T.: TEM analysis of the internal structures and mineralogy of Asian dust particles and the implications for optical modeling, *Atmos. Chem. Phys.*, 14, 7233–7254, doi:10.5194/acp-14-7233-2014, 2014.
- Jeong, G. Y., Park, M. Y., Kandler, K., Nousiainen, T., and Kempainen, O.: Mineralogical properties and internal structures of individual fine particles of Saharan dust, *Atmos. Chem. Phys.*, 16, 12397–12410, 690 doi:10.5194/acp-16-12397-2016, 2016.
- Jickells, T. D. An, Z. S. Andersena, K. K., Baker, A. R., Bergamettin, G. Brooks, N., Cao, J. J., Boyd, P. W., DUCE, R. A., and Torres, R.: Global iron connections between desert dust, ocean biogeochemistry, and climate, *Science*, 308, 67–71, doi: 10.1126/science.1105959, 2005.
- Journet, E., Desboeufs, K. V., Caquineau, S., and Colin, J. L.: Mineralogy as a critical factor of dust iron 695 solubility, *Geophys. Res. Lett.*, 35(L07805), doi:10.1029/2007GL031589, 2008.
- Kanawade, V. P., Srivastava, A. K., Ram, K., Asmi, E., Vakkari, V., Soni, V. K., Varaprasad, V., and Sarangi, C.: What caused severe air pollution episode of November 2016 in New Delhi? *Atmos. Environ.*, 222, 117125, doi: 10.1016/j.atmosenv.2019.117125, 2020.
- Kawamura, K. and Kaplan, I. R.: Motor exhaust emissions as a primary source for diocarboxylic acids in Los 700 Angeles ambient air, *Environ Sci. Technol.*, 21, 105–110, doi:10.1021/es00155a014, 1987.
- Kompalli, S. K., Babu, S. N. S., Moorthy, K. K., Satheesh, S. K., Gogoi, M. M., Nair, V. S., Jayachandran, V. N., Liu, D., Flynn, M. J., and Coe, H.: Mixing state of refractory black carbon aerosol in the South Asian outflow over the northern Indian Ocean during winter, *Atmos. Chem. Phys.*, 21, 9173–9199, 2, doi: 10.5194/acp-21-9173-2021, 2021.
- 705 Kukutschová, J., Moravec, P., Tomášek, V., Matějka, V., Smolík, J., Schwarz, J., Seidlerová, J., Safářová, K., and Filip, P.: On airborne nano/micro-sized wear particles released from low-metallic automotive brakes, *Environ. Pollut.*, 159(4), 998–1006, doi:10.1016/j.envpol.2010.11.036, 2011.



- Kumar, A. and Sarin, M.: Aerosol iron solubility in a semi-arid region: Temporal trend and impact of anthropogenic sources, *Tellus Ser. B Chem. Phys. Meteorol.*, 62, 125–132, doi: 10.1111/j.1600-0889.2009.00448.x, 2010.
- 710
- Li, W., Xu, L., Liu, X., Zhang, J., Lin, Y., Yao, X., Gao, H., Zhang, D., Chen, J., Wang, W., Harrison, R. M., Zhang, X., Shao, L., Fu, P., Nenes, A., and Shi, Z.: Air pollution – aerosol interactions produce more bioavailable iron for ocean ecosystems, *Sci. Adv.* 3, e1601749, doi:10.1126/sciadv.1601749, 2017.
- Liati, A., Pandurangi, S. S., Boulouchos, K., Schreiber, D., and Dasilva, Y. A. R.: Metal nanoparticles in diesel exhaust derived by in-cylinder melting of detached engine fragments, *Atmos. Environ.*, 101, 34–40, doi:10.1016/j.atmosenv.2014.11.014, 2015.
- 715
- Liu, M. and Matsui, H.: Aerosol radiative forcings induced by substantial changes in anthropogenic emissions in China from 2008 to 2016, *Atmos. Chem. Phys.*, 21, 5965–5982, doi:10.5194/acp-21-5965-2021, 2021a.
- Liu, M. and Matsui, H.: Improved simulations of global black carbon distributions by modifying wet scavenging processes in convective and mixed-phase clouds, *J. Geophys. Res.–Atmos.*, 126, e2020JD033890, doi:10.1029/2020JD033890, 2021b.
- 720
- Liu, M., Matsui, H., Hamilton, D., Lamb, K. D., Rathod, S. D., Schwarz, J. P., and Mahowald, N. M.: The underappreciated role of anthropogenic sources in atmospheric soluble iron flux to the Southern Ocean, *npj Clim. Atmos. Sci.*, 5, 28, doi: 10.1038/s41612-022-00250-w, 2022.
- 725
- Liu, H., Wang, Y., and Wendt, J. O.: Particle size distributions of fly ash arising from vaporized components of coal combustion: A comparison of theory and experiment, *Energy Fuels*, 32(4), 4300–4307, doi: 10.1021/acs.energyfuels.7b03126, 2018.
- Luo, C., Mahowald, N., Bond, T., Chuang, P. Y., Artaxo, P., Siefert, R., Chen, Y., and Schauer, J.: Combustion iron distribution and deposition, *Glob. Biogeochem. Cycles*, 22, GB1012, doi: 10.1029/2007GB002964, 2008.
- 730



- Machemer, S. D.: Characterization of airborne and bulk particulate from iron and steel manufacturing facilities, *Environ. Sci. Technol.*, 38(2), 381–389, doi:10.1021/es020897v, 2004.
- Mahowald, N. M., Baker, A. R., Bergametti, G., Brooks, N., Duce, R. A., Jickells, T. D., Kubilay, N., Prospero, J. M., and Tegen, I.: Atmospheric global dust cycle and iron inputs to the ocean, *Glob. Biogeochem. Cycles*, 19, GB402, 2005.
- 735
- Mahowald, N. M., Engelstaedter, S., Luo, C., Sealy, A., Artaxo, P., Benitez-Nelson, C., Bonnet, S., Chen, Y., Chuang, P. Y., Cohen, D. D., Dulac, F., Herut, B., Johansen, A. M., Kubilay, N., Losno, R., Maenhaut, W., Paytan, A., Prospero, J. M., Shank, L. M., and Siefert R. L.: Atmospheric Iron Deposition: Global Distribution, Variability, and Human Perturbations, *Annu. Rev. Marine. Sci.*, 1, 245–278, doi:10.1146/annurev.marine.010908.163727, 2009.
- 740
- Mahowald, N. M., Hamilton, D. S., Mackey, K. R. M., Moore, J. K., Baker, A. R., Scanza, R. A., and Zhang, Y.: Aerosol trace metal leaching and impacts on marine microorganisms, *Nature Communications*, 9(1), doi:10.1038/s41467-018-04970-7, 2018.
- Markowski, G. R. and Filby, R.: Trace Element Concentration as a Function of Particle Size in Fly Ash from a Pulverized Coal Utility Boiler, *Environ. Sci. Technol.*, 19, 796–804, doi:10.1021/es00139a005, 1985.
- 745
- Martin, J. H. and Fitzwater, S.: Iron deficiency limits phytoplankton growth in the north-east Pacific subarctic, *Nature*, 331, 947–975, 1988.
- Matsui, H.: Development of a global aerosol model using a two-dimensional sectional method: 1. Model design, *J. Adv. Model. Earth Syst.*, 9, 1921–1947, doi:10.1002/2017ms000936, 2017.
- 750
- Matsui, H.: Black carbon absorption efficiency under preindustrial and present-day conditions simulated by a size- and mixing-state-resolved global aerosol model, *J. Geophys. Res.–Atmos.*, 125, e2019JD032316, doi:10.1029/2019 JD032316, 2020.



- Matsui, H. and Mahowald, N.: Development of a global aerosol model using a two-dimensional sectional method: 2. Evaluation and sensitivity simulations, *J. Adv. Model. Earth Syst.*, 9, 1887–1920, doi:10.1002/2017ms000937, 2017.
- 755
- Matsui, H., Koike, M., Kondo, Y., Fast, J. D., and Takigawa, M.: Development of an aerosol microphysical module: Aerosol Two-dimensional bin module for foRmation and Aging Simulation (ATRAS), *Atmos. Chem. Phys.*, 14, 10315–10331, doi:10.5194/acp-14-10315-2014, 2014.
- Matsui, H., Hamilton, D. S., and Mahowald, N. M.: Black carbon radiative effects highly sensitive to emitted particle size when resolving mixing-state diversity, *Nat. Commun.*, 9, 3446, doi:10.1038/s41467-018-05635-1, 2018a.
- 760
- Matsui, H., Mahowald, N. M., Moteki, N., Hamilton, D. S., Ohata, S., Yoshida, A., Koike, M., Scanza, R. A., and Flanner, M. G.: Anthropogenic combustion iron as a complex climate forcer, *Nat. Commun.*, 9, 1593, doi:10.1038/s41467-018-03997-0, 2018b.
- 765
- Matsuki, A., Iwasaka, Y., Shi, G., Zhang, D., Trochkin, D., Yamada, M., Kim, Y.-S., Chen, B., Nagatani, T., Miyazawa, T., Nagatani, M., and Nakata, H.: Morphological and chemical modification of mineral dust: Observational insight into the heterogeneous uptake of acidic gases, *Geophys. Res. Lett.*, 32, L22806, doi:10.1029/2005GL024176, 2005.
- Miki, Y., Ueda, S., Miura, K., Furutani, H., and Uematsu, M.: Atmospheric Fe-containing particles over the North Pacific Ocean: The mixing states with water soluble materials, *Earozoru Kenkyu*, 29, 104–111, 2014.
- 770
- Mossop, S. C.: Stratospheric particles at 20 km, *Nature*, 199, 325–326, doi:10.1016/0016-7037(65)90017-7, 1963.
- Moteki, N., Adachi, K., Ohata, S., Yoshida, A., Harigaya, T., Koike, M., and Kondo, Y.: Anthropogenic iron oxide aerosols enhance atmospheric heating, *Nat. Commun.*, 8, 15329, doi: 10.1038/ncomms15329, 2017.
- 775
- Murr, L. E. and Soto, K. F.: A TEM study of soot, carbon nanotubes, and related fullerene nanopholyhedra in common fuel-gas combustion sources, *Mater. Charact.*, 55, 50–65. 2005.





- Myriokefalitakis, S., Ito, A., Kanakidou, M., Nenes, A., Krol, M. C., Mahowald, N. M., Scanza, R. A., Hamilton, D. S., Johnson, M. S., Meskhidze, N., Kok, J. F., Guieu, C., Baker, A. R., Jickells, T. D., Sarin, M. M., Bikkina, S., Shelley, R., Bowie, A., Perron, M. M. G., and Duce, R. A.: Reviews and syntheses: the  
780 GESAMP atmospheric iron deposition model intercomparison study, *Biogeosciences*, 15, 6659–6684, <https://doi.org/10.5194/bg-15-6659-2018>, 2018.
- Narukawa, M., Kawamura, K., Takeuchi, N., and Nakajima, T.: Distribution of dicarboxylic acids and carbon isotopic compositions in aerosols from 1997 Indonesian forest fires, *Geophys. Res. Lett.*, 26, 3101–3104, doi: 10.1029/1999GL010810, 1999.
- 785 Oakes, M., Ingall, E. D., Lai, B., Shafer, M. M., Hays, M. D., and Liu, Z. G.: Iron solubility related to particle sulfur content in source emission and ambient fine particles, *Environmental Science and Technology*, 46(12), 6637–6644, doi:10.1021/es300701c, 2012.
- Ohata, S., Yoshida, A., Moteki, N., Adachi, K., Takahashi, Y., Kurisu, M., and Koike, M.: Abundance of light-absorbing anthropogenic iron oxide aerosols in the urban atmosphere and their emission sources, *J. Geophys. Res. Atmos.*, 123, 8115–8134, doi:10.1029/2018 JD028363, 2018.
- 790 Ojha, N., Sharma, A., Kumar, M., Girach, I., Ansari, T. U., Sharma, S. K., Singh, N., Pozzer, A., and Gunthe, S. S.: On the widespread enhancement in fine particulate matter across the Indo-Gangetic Plain towards winter, *Sci. Rep.*, 10, 5862, 5862 doi:10.1038/s41598-020-62710-8, 2020.
- Okada, K.: Nature of individual hygroscopic particles in the urban atmosphere, *J. Meteor. Soc. Japan*, 61, 727–  
795 735, 1983.
- Okada, K. and Hitzenberger, R. M.: Mixing properties of individual submicrometer aerosol particles in Vienna, *Atmos. Environ.*, 35, 5617–5628, doi:10.1016/S1352-2310(01)00126-1, 2001.
- Okada, K., Naruse, H., Tanaka, T., Nemoto, O., Iwasaka, Y., Wu, P.-M., Ono, A., Duce, R. A., Uematsu, M., Merrill, J. T., and Arao, K.: X-ray spectrometry of individual Asian dust-storm particles over the Japanese



- 800 islands and the North Pacific Ocean, *Atmos. Environ.*, 24A, 1369–1378, doi: 10.1016/0960-1686(90)90043-M, 1990.
- Okada, K., Qin, Y., and Kai, K.: Elemental composition and mixing properties of atmospheric mineral particles collected in Hohhot, China. *Atmos. Res.*, 73, 45–67, doi: 10.1016/j.atmosres.2004.08.001, 2005.
- Rathod, S. D., Hamilton, D. S., Mahowald, N. M., Klimont, Z., Corbett, J. J., and Bond, T. C.: A mineralogy-  
805 based anthropogenic combustion-iron emission inventory, *J. Geophys. Res.–Atmos.*, 125, e2019JD032114. doi:10.1029/2019JD032114, 2020.
- Rolph, G., Stein, A., and Stunder, B.: Real-time Environmental Applications and Display sYstem: READY, *Environ. Modell. Softw.*, 95, 210–228, doi:10.1016/j.envsoft.2017.06.025, 2017.
- Sakata, K., Kurisu, M., Takeichi, Y., Sakaguchi, A., Tanimoto, H., Tamenori, Y., Matsuki, A., and Takahashi,  
810 Y.: Iron (Fe) speciation in size-fractionated aerosol particles in the Pacific Ocean: The role of organic complexation of Fe with humic-like substances in controlling Fe solubility, *Atmos. Chem. Phys.*, 22, 9461–9482, <https://doi.org/10.5194/acp-22-9461-2022>, 2022.
- Sanderson, P., Su, S. S., Chang, I. T. H., Delgado Saborit, J. M., Kepaptsoglou, D. M., Weber, R. J. M., and Harrison, R. M.: Characterisation of iron-rich atmospheric submicrometre particles in the roadside  
815 environment, *Atmos. Environ.*, 140, 167–175, doi:10.1016/j.atmosenv.2016.05.040, 2016.
- Scanza, R. A., Hamilton, D. S., Perez Garcia-Pando, C., Buck, C., Baker, A., and Mahowald, N. M.: Atmospheric processing of iron in mineral and combustion aerosols: development of an intermediate-complexity mechanism suitable for Earth system models, *Atmos. Chem. Phys.*, 18, 14175–14196, <https://doi.org/10.5194/acp-18-14175-2018>, 2018.
- 820 Schroth, A. W., Crusius, J., Sholkovitz, E. R., and Bostick, B. C.: Iron solubility driven by speciation in dust sources to the ocean, *Nature Geoscience*, 2(5), 337–340, doi:10.1038/ngeo501, 2009.



- Sedwick, P. N., Sholkovitz, E. R., and Church, T. M.: Impact of anthropogenic combustion emissions on the fractional solubility of aerosol iron: Evidence from the Sargasso Sea, *Geochem. Geophys. Geosyst.*, 8, Q10Q06, doi: 10.1029/2007GC001586, 2007.
- 825 Shi, Z., Krom, M. D., Bonneville, S., Baker, A. R., Jickells, T. D., and Benning, L. G.: Formation of iron nanoparticles and increase in iron reactivity in mineral dust during simulated cloud processing, *Environ. Sci. Technol.*, 43, 6592–6596, 2009.
- Shi, Z., Krom, M. D., Bonneville, S., and Benning, L. G.: Atmospheric processing outside clouds increases soluble iron in mineral dust, *Environ. Sci. Technol.*, 49, 1472–1477, 2015.
- 830 Shi, Z., Krom, M. D., Jickells, T. D., Bonneville, S., Carslaw, K. S., Mihalopoulos, N., Baker, A. R., and Benning, L. G.: Impacts on iron solubility in the mineral dust by processes in the source region and the atmosphere: a review, *Aeolian Res.*, 5, 21–42, doi: 10.1016/j.aeolia.2012.03.001, 2012.
- Stein, A. F., Draxler, R. R., Rolph, G. D., Stunder, B. J. B., Cohen, M. D., and Ngan, F.: NOAA’s HYSPLIT atmospheric transport and dispersion modeling system, *B. Am. Meteorol. Soc.*, 96, 2059–2077, doi:10.1175/BAMS-D-14-00110.1, 2015.
- 835 Szumiata, T., Gzik-Szumiata, M., Brzózka, K., Górka, B., Gawroński, M., Świetlik, R., and Trojanowska, M.: Iron-containing phases in fly ashes from different combustion systems, *Nukleonika*, 60(1), 151–154, doi:10.1515/nuka-2015-0030, 2015.
- Takahashi, Y., Furukawa, T., Kanai, Y., Uematsu, M., Zheng, G., and Marcus, M. A.: Seasonal changes in Fe species and soluble Fe concentration in the atmosphere in the Northwest Pacific region based on the analysis of aerosols collected in Tsukuba, Japan, *Atmos. Chem. Phys.*, 13, 7695–7710, <https://doi.org/10.5194/acp-13-7695-2013>, 2013.
- 840 Takigawa, M., Patra, P. K., Matsumi, Y., Dhaka, S. K., Nakayama, T., Yamaji, K., Kajino, M., and Hayashida, S.: Can Delhi’s pollution be affected by crop fires in the Punjab Region? *SOLA*, 16, 86–91, doi: 10.2151/sola.2020-015, 2020.
- 845



- Tomeczek, J. and Palugniok, H.: Kinetics of mineral matter transformation during coal combustion, *Fuel*, 81(10), 1251–1258. doi: 10.1016/S0016-2361(02)00027-3, 2002
- Tsuda, A., Takeda, S., Saito, H., Nishioka, J., Kudo, I., Nojiri, Y., Suzuki, K., Uematsu, M., Wells, M. L., Tsumune, D., Yoshimura, Y., Aono, T., Aramaki, T., Cochlan, W. P., Hayakawa, M., Imai, K., Isada, T.,  
850 Iwamoto, Y., Johnson, W. K., Kameyama, S., Kato, S., Kiyosawa, H., Kondo, Y., Lévassieur, M., Machida, R. J., Nagao, I., Nakagawa, F., Nakanishi, T., Nakatsuka, S., Narita, A., Noiri, Y., Obata, H., Ogawa, H., Oguma, K., Ono, T., Sakuragi, T., Sasakawa, M., Sato, M., Shimamoto, A., Takata, H., Trick, C. G., Watanabe, Y. W., Wong, C. S., and Yoshie, N.: Evidence for the grazing hypothesis: grazing reduces phytoplankton responses of the HNLC ecosystem to iron enrichment in the Western Subarctic Pacific  
855 (SEED II), *Journal of Oceanography*, 63, 983–994, doi: 10.1007/s10872-007-0082-x, 2007.
- Tsuda, A., Takeda, S., Saito, H., Nishioka, J., Nojiri, Y., Kudo, I., Kiyosawa, H., Shiomoto, A., Imai, K., Ono, T., Shimamoto, A., Tsumune, D., Yoshimura, T., Aono, T., Hinuma, A., Kinugasa, M., Suzuki, K., Sohrin, Y., Noiri, Y., Tani, H., Deguchi, Y., Tsurushima, N., Ogawa, H., Fukami, K., Kuma, K., and Saino, T.: A mesoscale iron enrichment in the Western Subarctic Pacific induces a large centric diatom  
860 bloom, *Science*, 300, 958–961, doi:10.1126/science.10820, 2003.
- Ueda, S.: Morphological change of solid ammonium sulfate particles below the deliquescence relative humidity: Experimental reproduction of atmospheric sulfate particle shapes, *Aerosol Sci. Technol.*, 55, 423–437, doi: 10.1080/02786826.2020.1864277, 2021.
- Ueda, S., Hirose, Y., Miura, K., and Okochi, H.: Individual aerosol particles in and below clouds along a Mt.  
865 Fuji slope: Modification of sea-salt-containing particles by in-cloud processing, *Atmos. Res.*, 137, 216–227, D17207, doi:10.1016/j.atmosres.2010.10.021, 2014.
- Ueda, S., Miki, Y., Kato, H., Miura, K., Nakayama, H., Furutani, H., and Uematsu, M.: Internal structure of Asian dust particles over the western North Pacific: analyses using focused ion beam and transmission electron microscopy, *Atmosphere*, 11, doi:10.3390/atmos11010078, 2020.



- 870 Ueda, S., Miura, K., Kawata, R., Furutani, H., Uematsu, M., Omori, Y., and Tanimoto, H.: Number–size  
distribution of aerosol particles and new particle formation events in tropical and subtropical Pacific Oceans,  
*Atmospheric Environment*, 142, 324–339, doi:10.1016/j.atmosenv.2016.07.055, 2016
- Ueda, S., Mori, T., Iwamoto, Y., Ushikubo, Y., and Miura, K.: Wetting properties of fresh urban soot particles:  
Evaluation based on critical supersaturation and observation of surface trace materials, *Science of the Total*  
875 *Environment*, 811, doi:10.1016/j.scitotenv.2021.152274, 2022.
- Ueda, S., Nakayama, T., Taketani, F., Adachi, K., Matsuki, A., Iwamoto, Y., Sadanaga, Y., and Matsumi, Y.:  
Light absorption and morphological properties of soot-containing aerosols observed at an East Asian  
outflow site, Noto Peninsula, Japan, *Atmos. Chem. Phys.*, 16, 2525–2541, doi:10.5194/acp-16-2525-2016,  
2016.
- 880 Ueda, S., Osada, K., and Okada, K.: Mixing states of cloud interstitial particles between water-soluble and  
insoluble materials at Mt. Tateyama, Japan: Effect of meteorological conditions, *Atmos. Res.*, 99, 325–336,  
doi:10.1016/j.atmosres.2010.10.021, 2011a.
- Ueda, S., Osada, K., and Takami, A.: Morphological features of soot-containing particles internally mixed with  
water-soluble materials in continental outflow observed at Cape Hedo, Okinawa, Japan, *J. Geophys. Res.*,  
885 116, doi: 10.1029/2010 JD015565, 2011b.
- Uematsu, M., Duce, R. A., Prospero, J. M., Chen, L., Merrill, J. T., and McDonald, R. L. Transport of mineral  
aerosol from Asia over the North Pacific Ocean, *J. Geophys. Res.*, 88(C9), 5343–5352,  
doi:10.1029/JC088iC09p05343, 1893.
- Umo, N. S., Wagner, R., Ullrich, R., Kiselev, A., Saathoff, H., Weidler, P. G., Cziczo, D. J., Leisner, T., and  
890 Möhler, O.: Enhanced ice nucleation activity of coal fly ash aerosol particles initiated by ice-filled pores,  
*Atmos. Chem. Phys.*, 19, 8783–8800, <https://doi.org/10.5194/acp-19-8783-2019>, 2019.



- Waanders, F. B., Vinken, E., Mans, A., and Mulaba-Bafubiandi, A. F.: Iron minerals in coal, weathered coal and coal Ash - SEM and Mössbauer Results, *Hyperfine Interactions*, 148–149(1–4), 21–29, doi:10.1023/B:HYPE.0000003760.89706.f6, 2003.
- 895 Waller, R. E., Brooks, A. G. F., and Cartwright, J.: An electron microscope study of particles in town air, *J. Air Wet. Pollut.*, 7, 779–785, 1963.
- Wang, R., Balkanski, Y., Boucher, O., Bopp, L., Chappell, A., Ciaï, P., Hauglustaine, D., Peñuelas, J., and Tao, S.: Sources, transport and deposition of iron in the global atmosphere, *Atmos. Chem. Phys.*, 15, 6247–6270, <https://doi.org/10.5194/acp-15-6247-2015>, 2015.
- 900 Wiederhold, J. G., Kraemer, S. M., Teutsch, N., Borer, P. M., Halliday, A. N., and Kretzschmar, R.: Iron isotope fractionation during proton-promoted, ligand-controlled, and reductive dissolution of goethite, *Environ. Sci. Technol.*, 40, 3787–3793, 2006.
- Yao, Z. T., Ji, X. S., Sarker, P. K., Tang, J. H., Ge, L. Q., Xia, M. S., and Xi, Y. Q.: A comprehensive review on the applications of coal fly ash, *Earth Sci. Rev.*, 141, 105–121, doi: 10.1016/j.earscirev.2014.11.016, 905 2015.
- Zhang, D. and Iwasaka, Y.: Nitrate and sulfate in individual Asian dust-storm particles in Beijing, China in spring of 1995 and 1996, *Atmos. Environ.*, 33, 3213–3223, doi: 10.1016/S1352-2310(99)00116-8, 1999.